/N-37-:-/2.

Bureau of Engineering Research
The University of Texas at Austin
Austin, Texas

CAR 97-1

SUBSTRUCTURE SYSTEM IDENTIFICATION FOR FINITE ELEMENT MODEL UPDATING
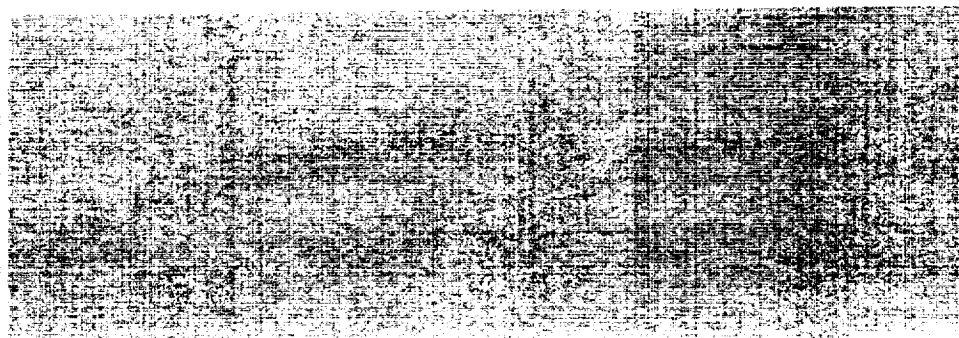by
Roy R. Craig, Jr. and Eric L. Blades

ABSTRACT

This report summarizes research conducted under NASA Grant NAG8-1130 on the topic "Substructure System Identification for Finite Element Model Updating." It covers the period of the grant from April 19, 1995 until August 31, 1996. The research concerns ongoing development of the Substructure System Identification Algorithm (SSID Algorithm), a system identification algorithm that can be used to obtain mathematical models of substructures, like Space Shuttle payloads. In the present study, particular attention was given to the following topics: making the algorithm robust to noisy test data, extending the algorithm to accept experimental FRF data that covers a broad frequency bandwidth, and developing a test analytical model (TAM) for use in relating test data to reduced-order finite element models.

This report summarizes research described in the following technical report and papers and presents some overall conclusions and recommendations.

Bound Technical Report

- Blades, E. L., and Craig, R. R., Jr., *A Frequency-Domain Substructure System Identification Algorithm*, Ref. [1].

Papers Presented at Technical Meetings

- Craig, R., and Blades, E., "Substructure System Identification – Reduced-Order Models," Ref. [2].

- Blades, E. L., and Craig, R. R., Jr., "Frequency-Domain Substructure System Identification," Ref. [3].

- Blades, E. L., and Craig, R. R., Jr., "A Craig-Bampton Test-Analysis Model," Ref. [4].

- Craig, R. R., Jr., and Blades, E. L., "A Band-Processing Algorithm for Structural System Identification," Ref. [5].

SUBSTRUCTURE SYSTEM IDENTIFICATION

FOR FINITE ELEMENT MODEL UPDATING

by

Roy R. Craig, Jr.*

Eric L. Blades†

Center for Aeromechanics Research

(formerly Center for Aeronautical Research)

Bureau of Engineering Research

College of Engineering

The University of Texas at Austin

Austin, Texas 78712

February 1997

---

*John J. McKetta Energy Professor in Engineering

†Engineer, Structural Dynamics Research Corporation, formerly Graduate Student, Aerospace Engineering

ACKNOWLEDGEMENTS

TABLE OF CONTENTS

Chapter 1

INTRODUCTION

This report summarizes the research accomplished in the Structural Dynamics Laboratory of the Department of Aerospace Engineering and Engineering Mechanics at The University of Texas at Austin under the sponsorship of NASA Grant NAG8-1130. Under the sponsorship of NASA Grant NAG9-670 with NASA Johnson Space Center, the author, together with graduate students Wiede Cutshall and Eric Blades, developed a "preliminary" version of the Substructure System Identification Algorithm, an algorithm for reducing FRFs from a vibration test to test-derived mass, damping, and stiffness matrices. The major research accomplishments under that grant are described in the reports and presentations listed in Refs. [6-10]. Reference [7] summarizes that work. At the conclusion of that work, a version of the SSID algorithm had been developed that was capable of identifying M, C, and K matrices from simulated noise-free FRFs of acceleration responses at all degrees of freedom of the model and FRFs for reaction-forces. Reference [10] describes early efforts to identify reduced-order models from "noisy" FRFs. That work indicated that the SSID algorithm was not yet robust enough to identify correct reduced-order mass, damping, and stiffness matrices for other than very-low-order models ($\leq$ 10 DOF).

In the present study particular attention was given to the following top-

ics: making the algorithm robust to noisy test data, extending the algorithm to accept FRF data that covers a broad bandwidth, and developing a test analytical model (TAM) for use in relating test data to finite element models in the Craig-Bampton format [11].

The stated goals for this research were:

1. to develop a version of the SSID algorithm that incorporates model reduction, and to relate SSID-identified substructure math models to reduced-order finite-element-based Craig-Bampton math models, thus demonstrating test verification of Craig-Bampton models; and

2. to use laboratory tests and simulation studies to assess the feasibility of conducting a full-scale Space Shuttle Payload test using the extended SSID method.

To achieve the above-stated goals the following two tasks were proposed:

1. Incorporate model reduction into the present SSID algorithm to obtain an algorithm for Substructure System Identification with Model Reduction (SSID-MR).

2. Apply the SSID-MR substructure identification method developed in Task 1 by performing simulation studies and by conducting vibration tests of representative substructure hardware. Develop a preliminary test/analysis plan for applying SSID-MR procedures in an actual payload model-verification test.

Chapter 2 of this report reviews the basic SSID Algorithm, while Chapt. 3 presents extended abstracts of the technical papers and report covering research under the present grant. Conclusions based on this research are given in Chapt. 4. A sample computer run is provided in Appendix A.

Chapter 2

BASIC SUBSTRUCTURE SYSTEM
IDENTIFICATION ALGORITHM

To introduce the SSID Algorithm, Chapt. 3 of Ref. [1], which summarizes
the basic SSID algorithm, is reproduced in the present chapter. The major new
research accomplishments are described in the publications and presentations
that are summarized in Chapt. 3 of this report.

2.1   Introduction

The SSID Algorithm is a new frequency-domain identification method
that can be used to obtain a linear viscous-damped model of a substructure[1].
Every interface degree of freedom is either actively excited by a shaker with
the input measured or is supported by the test stand with the reaction forces
measured. The substructure is "isolated" from the test stand by measuring
the reaction force; thus the substructure can be identified. In addition, test-
stand dynamics are automatically taken into account, so there is no need for
a separate modal test or for a finite element model of the test stand. This
procedure makes it possible to obtain not only the fixed-interface modal data
for a Craig-Bampton substructure model, but also the data associated with the

---

[1]Although designed especially to facilitate accurate testing of substructures, the algorithm
can be considered to be a "general-purpose" structural system identification algorithm.

constraint modes.

An overview of the theoretical derivation of the proposed SSID Algorithm, which is a two-step identification process, is provided in this chapter. A complete description of the algorithm is given in Ref. [6].

2.2 Identification of $M^{-1}C$ and $M^{-1}K$

Assume that the substructure has viscous damping and that the total number of motion transducers (accelerometers) is at least twice the expected number of normal modes in the frequency range of interest[2]. Every interface degree of freedom is to have a co-located actuator/sensor (force/accelerometer) pair. In addition, there are to be motion sensors (accelerometers) at selected interior degrees of freedom.

Let the equations of motion in physical coordinates and the output equation be

$$M\ddot{x} + C\dot{x} + Kx = Dp(t)$$
$$y = S\ddot{x} \tag{2.1}$$

where $x \in R^{N_x}$ is the displacement vector; $p \in R^{N_p}$ is the input force vector; $y \in R^{N_y}$ is the output measurement vector; M, C, and K are the system mass, damping, and stiffness matrices, respectively; D is the force distribution matrix; and S is the acceleration sensor distribution matrix. For the present discussion, we will assume that the above N_x-degree-of-freedom model represents a

---

[2]This restriction may be relaxed by the method described in Sect. 3.3.1.

reduced-order model of the structure. Let the coordinates be partitioned in the following manner:

$$x \equiv \left\{ \begin{array}{c} x_i \\ x_b \end{array} \right\} \equiv \left\{ \begin{array}{c} x_i \\ x_f \\ x_r \end{array} \right\} \tag{2.2}$$

where f stands for forced DOFs (i.e., DOFs where there is an active force input); r stands for reaction DOFs (i.e., interface DOFs where the tested substructure reacts against the support structure); i stands for interior DOFs (i.e., DOFs where neither an active force is applied nor a reaction is measured); and b stands for boundary DOFs, the combination of f-coordinates and r-coordinates. These sets of coordinates are illustrated in Fig. 2.1.
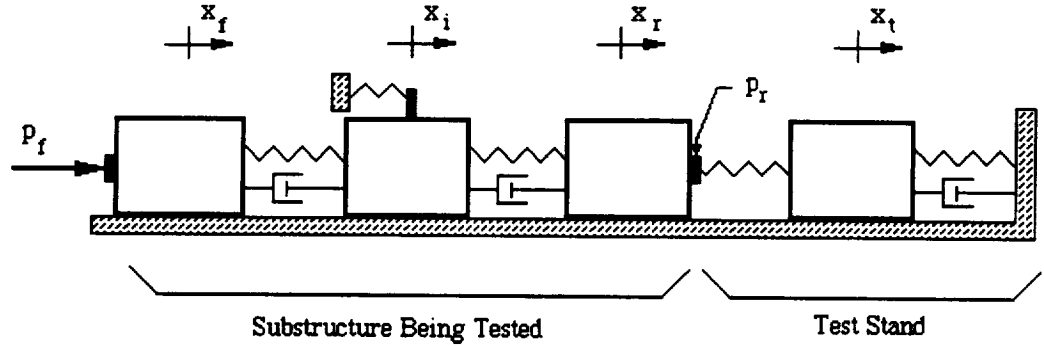
Figure 2.1: Substructure Model – Vibration Test Configuration

Equation 2.1a can be written in the following partitioned form (damping is omitted here):

$$\begin{bmatrix} M_{ii} & M_{if} & M_{ir} \\ M_{fi} & M_{ff} & M_{fr} \\ M_{ri} & M_{rf} & M_{rr} \end{bmatrix} \left\{ \begin{array}{c} \ddot{x}_i \\ \ddot{x}_f \\ \ddot{x}_r \end{array} \right\} + \begin{bmatrix} K_{ii} & K_{if} & K_{ir} \\ K_{fi} & K_{ff} & K_{fr} \\ K_{ri} & K_{rf} & K_{rr} \end{bmatrix} \left\{ \begin{array}{c} x_i \\ x_f \\ x_r \end{array} \right\} = [D] p(t) \tag{2.3}$$

Let us consider the complex frequency response of the substructure due to excitation at frequency ω_k, but with the interior DOFs force-free. Then,

$$p_k(t) \equiv \left\{ \begin{array}{c} p_f(t) \\ p_r(t) \end{array} \right\}_k = P(\omega_k)e^{j\omega_k t} \equiv \left\{ \begin{array}{c} F(\omega_k) \\ R(\omega_k) \end{array} \right\} e^{j\omega_k t} \qquad (2.4)$$

(From Eq. 2.4 onward, the vectors can be complex.) The complex displacement response can be written as

$$x_k(t) = X(\omega_k)e^{j\omega_k t} \qquad (2.5)$$

and similar expressions can be obtained for velocity, etc. Then, the frequency-domain version of Eq. 2.1a is

$$\left[M + \left(\frac{1}{j\omega_k} \right) C + \left(\frac{1}{-\omega_k^2} \right) K \right] A(\omega_k) = \left[\begin{array}{cc} D_f & D_r \end{array} \right] \left\{ \begin{array}{c} F(\omega_k) \\ R(\omega_k) \end{array} \right\} \qquad (2.6)$$

The experimental data input to the algorithm is complex, but the system matrices to be identified are real. To insure that real matrices will be determined, a procedure from Ref. [12] is used. After some algebraic manipulation, the following equation is obtained for estimating the matrices $\hat{C}$, $\hat{K}$, $\hat{D}_f$ and $\hat{D}_r$:

$$\left[\begin{array}{cccc} \hat{C} & \hat{K} & \hat{D}_f & \hat{D}_r \end{array} \right] \left[\begin{array}{cc} \Re\left[\dfrac{H_{af}}{j\omega} \right] & \Im\left[\dfrac{H_{af}}{j\omega} \right] \\ \Re\left[\dfrac{H_{af}}{-\omega^2} \right] & \Im\left[\dfrac{H_{af}}{-\omega^2} \right] \\ -\Re[H_{ff}] & -\Im[H_{ff}] \\ -\Re[H_{rf}] & -\Im[H_{rf}] \end{array} \right] = \left[\begin{array}{cc} -\Re[H_{af}] & -\Im[H_{af}] \end{array} \right] \qquad (2.7)$$

8

where

$$\hat{C} = M^{-1}C \quad, \quad \hat{K} = M^{-1}K \quad, \quad \hat{D}_f = M^{-1}D_f \quad, \quad \text{and} \quad \hat{D}_r = M^{-1}D_r \quad (2.8)$$

and the H matrices are measured frequency response function (FRF) matrices and $\Re[\cdot]$ and $\Im[\cdot]$ denote the real part and the imaginary part of the given quantity, respectively. The data used in Eq. 2.7 is stacked in the following manner:

$$\left[\frac{H_{af}}{j\omega}\right] \equiv \begin{bmatrix} \frac{1}{j\omega_1}H_{a_1f_1}(\omega_1) & \cdots & \frac{1}{j\omega_1}H_{a_1f_{N_f}}(\omega_1) & \cdots & \frac{1}{j\omega_{N_\omega}}H_{a_1f_{N_f}}(\omega_{N_\omega}) \\ \frac{1}{j\omega_1}H_{a_2f_1}(\omega_1) & \cdots & \frac{1}{j\omega_1}H_{a_2f_{N_f}}(\omega_1) & \cdots & \frac{1}{j\omega_{N_\omega}}H_{a_2f_{N_f}}(\omega_{N_\omega}) \\ & & \vdots & & \\ \frac{1}{j\omega_1}H_{a_{N_x}f_1}(\omega_1) & \cdots & \frac{1}{j\omega_1}H_{a_{N_x}f_{N_f}}(\omega_1) & \cdots & \frac{1}{j\omega_{N_\omega}}H_{a_{N_x}f_{N_f}}(\omega_{N_\omega}) \end{bmatrix}$$

$$(2.9)$$

The other partitions of the data in Eq. 2.7 are formed similarly.

A least-squares solution of Eq. 2.7 is required. A further discussion of least-squares solution procedures is given in Sect. 3.2.

2.3   Identification of M, C, and K

In the previous section, an algorithm was described for identifying the system matrices $\hat{C}$, $\hat{K}$, and $\hat{D}$, which are defined by Eqs. 2.7. From the system matrices $\hat{C}$, $\hat{K}$, and $\hat{D}$, we wish to determine the system matrices M, C, K, and D, especially the first three. The first step is to perform an eigensolution using the matrices identified from Eq. 2.7. Let $N_s \equiv 2N_x$, and let us define the state variable

$$z \equiv \left\{ \begin{array}{c} x \\ \dot{x} \end{array} \right\} \tag{2.10}$$

and state matrices

$$\hat{A}_s = \left[\begin{array}{cc} \hat{C} & I \\ I & 0 \end{array} \right], \quad \hat{B}_s = \left[\begin{array}{cc} \hat{K} & 0 \\ 0 & -I \end{array} \right], \quad \hat{D}_s = \left[\begin{array}{c} \hat{D} \\ 0 \end{array} \right] \tag{2.11}$$

Then the following eigenproblem is solved for the complex eigenvalues λ_r and the complex eigenvectors $\hat{\theta}_r$:

$$[\lambda_r \hat{A}_s + \hat{B}_s]\hat{\theta}_r = 0 \qquad r = 1, \ldots, N_s \tag{2.12}$$

To determine the system matrices M, C, and K, a mode-superposition representation of the complex frequency response can be employed. Using the eigenvectors, $\hat{\theta}_r$, let the mode-superposition solution for the states z be

$$z(t) = \sum_{r=1}^{N_s} \hat{\theta}_r \gamma_r(t) = \hat{\Theta}\Gamma(t) \tag{2.13}$$

where orthogonality holds in the following form:

$$\hat{\Theta}^T A_s \hat{\Theta} = \text{diag}(\tilde{a}_r), \quad \hat{\Theta}^T B_s \hat{\Theta} = \text{diag}(\tilde{b}_r) \tag{2.14}$$

with

$$A_s = \left[\begin{array}{cc} C & M \\ M & 0 \end{array} \right], \quad B_s = \left[\begin{array}{cc} K & 0 \\ 0 & -M \end{array} \right] \tag{2.15}$$

The following modal-response equations are obtained:

$$\tilde{a}_r \dot{\gamma}_r(t) + \tilde{b}_r \gamma_r(t) = \hat{\theta}_r^T D_s p(t) \tag{2.16}$$

10

The mode-superposition solution leads, eventually, to the following acceleration frequency response:

$$A_k = -\omega_k^2 X_k = \sum_{r=1}^{N_s} \left(\frac{1}{\tilde{a}_r} \right) \left[R_{kr} \left\{ \hat{\theta}_x \right\}_r \left\{ \hat{\theta}_x \right\}_r^T \right] D P_k \qquad (2.17)$$

where

$$P_k \equiv \left\{ \begin{array}{c} F(\omega_k) \\ R(\omega_k) \end{array} \right\} \qquad (2.18)$$

$$R_{kr} = \left(\frac{-\omega_k^2}{j\omega_k - \lambda_r} \right) \qquad (2.19)$$

As in the derivation of Eq. 2.7, assume that averaged frequency-response data are available at N_ω frequencies, so Eq. 2.17, averaged at each of these frequencies, leads to the following equation:

$$G_{af} = \sum_{r=1}^{N_s} \left(\frac{1}{\tilde{a}_r} \right) \left[R_{kr} \left\{ \hat{\theta}_x \right\}_r \left\{ \hat{\theta}_x \right\}_r^T \right] [D_f D_r] \left[\begin{array}{c} G_{ff} \\ G_{rf} \end{array} \right] \qquad (2.20)$$

If Eq. 2.20 is postmultiplied by G_{ff}^{-1}, the following expression for the accelerance FRF matrix is obtained:

$$H_{af}(\omega_k) = \sum_{r=1}^{N_s} \left(\frac{1}{\tilde{a}_r} \right) \left[R_{kr} \left\{ \hat{\theta}_x \right\}_r \left\{ \hat{\theta}_x \right\}_r^T \right] [D_f D_r] \left[\begin{array}{c} I_{ff} \\ H_{rf} \end{array} \right] \qquad (2.21)$$

Now, the left-hand and right-hand sides of Eq. 2.21 are matrices of dimension $N_x \times N_f$. Let f_j indicate the jth column of each side of this equation. Then, write the jth column of Eq. 2.21 in the form

$$H_{af_j} = \sum_{r=1}^{N_s} \left(\frac{1}{\tilde{a}_r} \right) \left[R_{kr} \left\{ \hat{\theta}_x \right\}_r \left\{ \hat{\theta}_x \right\}_r^T \right] [D_f D_r] \left\{ \begin{array}{c} I_{ff_j} \\ H_{rf_j} \end{array} \right\} \qquad (2.22)$$

Finally, let Eq. 2.22 be repeated for each of the N_ω frequencies and N_f forces, and the resulting equations stacked vertically to form the following equation:

$$\left\{ \begin{array}{c} \left\{ \begin{array}{c} H_{af_1}(\omega_1) \\ \vdots \\ H_{af_1}(\omega_{N_\omega}) \end{array} \right\} \\ \vdots \\ \left\{ \begin{array}{c} H_{af_{N_f}}(\omega_1) \\ \vdots \\ H_{af_{N_f}}(\omega_{N_\omega}) \end{array} \right\} \end{array} \right\} = \left[\begin{array}{c} \left[\begin{array}{cccc} E_{11} & E_{12} & \ldots & E_{1,N_s} \\ & & \vdots & \\ E_{N_\omega,1} & E_{N_\omega,2} & \ldots & E_{N_\omega,N_s} \end{array} \right]_{f_1} \\ \vdots \\ \left[\begin{array}{cccc} E_{11} & E_{12} & \ldots & E_{1,N_s} \\ & & \vdots & \\ E_{N_\omega,1} & E_{N_\omega,2} & \ldots & E_{N_\omega,N_s} \end{array} \right]_{f_{N_f}} \end{array} \right] \left\{ \begin{array}{c} 1/\tilde{a}_1 \\ \vdots \\ 1/\tilde{a}_{N_s} \end{array} \right\}$$

$$(2.23)$$

where

$$[E_{kr}]_{f_j} = \left[R_{kr} \left\{ \hat{\theta}_x \right\}_r \left\{ \hat{\theta}_x \right\}_r^T \right] \left\{ D_{f_j} + D_r H_{rf_j} \right\} \tag{2.24}$$

Equation 2.23 is the key equation that is required to estimate the system matrices M, C, and K. It is used to obtain least squares estimates of the N_s modal parameters $\tilde{a}_r$. The corresponding modal parameters $\tilde{b}_r$ can then be computed from

$$\tilde{b}_r = -\lambda_r \tilde{a}_r \qquad r = 1, \ldots, N_s \tag{2.25}$$

With these values of $\tilde{a}_r$ and $\tilde{b}_r$, the state matrices A_s and B_s, defined by Eqs. 2.15, are computed by using Eqs. 2.14, written in the form

$$\begin{aligned} A_s &= \hat{\Theta}^{-T} \text{diag}(\tilde{a}_r) \hat{\Theta}^{-1} \\ B_s &= \hat{\Theta}^{-T} \text{diag}(\tilde{b}_r) \hat{\Theta}^{-1} \end{aligned} \tag{2.26}$$

Finally, the system matrices M, C, and K are obtained by referring to Eqs. 2.15 and extracting the appropriate partitions of the A_s and B_s matrices that are obtained from Eq. 2.26.

Chapter 3

ABSTRACTS OF TECHNICAL PAPERS AND REPORTS

Extended abstracts of publications describing research conducted under the subject grant are presented in this chapter.

3.1 A Frequency-Domain Substructure System Identification Algorithm – (Ref. [1])

Reference [1] describes the research that was conducted on the SSID Algorithm under the present grant. Various aspects of this research were discussed in presentations at technical meetings (Refs. [2-5]).

As previously noted, Chapt. 3 of Ref. [1] summarizes the basic SSID Algorithm. Chapter 4 is a development of a test-analytical model (TAM) based on the Craig-Bampton reduced-order component mode synthesis (CMS) model. This CB-TAM, in contrast to other TAMs like the Guyan-Irons TAM, permits analytical Craig-Bampton models to be more directly compared to test data. Reference [4] is based on this chapter.

Chapters 5 and 6 of Ref. [1] discuss the remaining four major topics that were studied: full-order and reduced-order models from noise-free data, least-squares solution methods for processing noisy data, narrow-band data processing, and use of pseudo DOFs to expand model order. The simulation

13

studies presented in Chapt. 6 were based on a 52-DOF NASTRAN model of the "payload simulator" shown in Fig. 3.1.

Figure 3.1: Payload Simulator Finite Element Model

The following conclusions were reached:
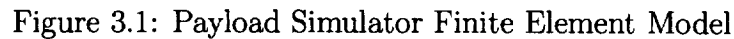
- The SSID Algorithm identified to within 0.25% all elements of the full-order mass, damping, and stiffness matrices of a 52-DOF structure from noise-free simulated test data. The input consisted of one applied force and two applied moments.

- The effects of spatial truncation (limited number of accelerometers) and frequency truncation (limited frequency bandwidth) were studied. Based on the results obtained for 10-DOF, 12-DOF, and 16-DOF reduced-order models of the 52-DOF structure, it was concluded that the algorithm is capable of identifying valid reduced-order structural models from noise-free data. However, the best estimation of a reduced-order model of a

given order is obtained when the input frequency range contains only the corresponding number of modes.

- Three least-squares methods, *ordinary least-squares* (OLS), *total least-squares* (TLS), and *scaled total least-squares* (STLS), were used to solve the over-determined system of linear equations, Eq. 2.7. No acceptable solution for any of the reduced-order models was ever obtained when the OLS method was used. Both the TLS method and the STLS method successfully identified 10-DOF and 12-DOF reduced-order models of the 52-DOF structure. However, none of the three solution methods obtained an acceptable 16-DOF reduced-order model from noisy data, a situation that led to the study of band processing of the data.

- A technique called *band processing* was shown to successfully identify reduced-order structural models from noisy broad-bandwidth FRF data.

- Pseudo degrees of freedom were examined as a way to expand the model size when there are fewer output sensors than there are modes present in the data.

- The system matrices identified by the SSID algorithm were compared to other test-analysis models, and it was found that the SSID reduced-order models represent the dynamic characteristics of the structure as well as, if not better than, the other TAMs do.

- The SSID reduced-order models provide the information necessary to obtain the fixed-interface modal data associated with the Craig-Bampton

substructure model and also the data associated with the constraint modes.

3.2 Substructure System Identification – Reduced-Order Models – (Ref. [2])

This paper describes the performance of various least-squares equation solvers used for identifying reduced-order models from noisy test data. The theory part of the paper is based on Sect. 5.1 of Ref. [1]. The simulations described in the paper are based on an 18-DOF Z-translation-only model of the payload simulator shown in Fig. 3.1.

3.2.1 Least-Squares Equation Solvers

The ordinary least-squares (OLS) method and the more recent total least-squares (TLS) method are mathematical modeling procedures used to solve an under-determined or over-determined system of linear equations. Both parameter identifications, Eqs. 2.7 and 2.23, can be cast in the form

$$AX \approx B \qquad (3.1)$$

The approximate sign is used to emphasize that the data is contaminated by noise. If there is no noise in the data, then Eq. 3.1 will be an equality. The OLS method and the TLS method seek solutions that minimizes the error between the true system model and the measured data.

Perhaps the best known method of solution for an over-determined system of linear equations is the OLS method. For simplicity, consider the case

when $d = 1$. In the OLS approach, the measurements of the variables in the data matrix A are assumed to be free of error, and all errors are assumed to be confined to the observation vector b. The OLS method will result in an unbiased estimate if the error model is of the form

$$Ax \approx \{b_0 + \Delta b\} \tag{3.2}$$

The TLS method [13] produces estimates that are generated from a system of linear equations where it is assumed that both the data matrix A and the observation vector b contain errors. The error model for the TLS method is of the form

$$[A_0 + \Delta A]\{x\} \approx \{b_0 + \Delta b\} \tag{3.3}$$

Further details concerning these least-squares methods is given in Sect. 5.1 of Ref. [1]

3.2.2 Numerical Examples

Simulated noisy test data was used to assess the ability of the SSID system-identification procedure, with OLS and TLS solvers, to identify valid reduced-order models. A finite element (FE) model of the parallel-beam "payload simulator" in Fig. 3.1, reduced from 54 DOFs to the 18 Z-translational DOFs, was used as the "true" system. Modal damping at a level of 2% was added to obtain a damping matrix for the FE model. The payload simulator was hung from soft springs ("bungee cords") at nodes 11, 13, 14, and 16; and was excited in the z direction at all three interface nodes: 4, 8, and 18. Iden-

tification of both a full-order model and a reduced-order model are illustrated. In the latter case, OLS results and TLS results are compared.

Identification of the Full-Order Model

The first simulation was of the full-order model without any noise on the simulated FRF data. The SSID identification was based on 256 frequency lines uniformly spaced from 0.5 Hz to 2000 Hz. The undamped natural frequencies of the 18-DOF system, which range from 1.15 Hz to 8597 Hz, were all identified exactly (to within 7-digit accuracy), even though two of the undamped natural frequencies are well above the 2000 Hz upper limit of the FRF data. All simulations were programmed using MATLAB[TM][14].

Figures 3.2a through 3.2c show the percent errors in individual terms of the mass, damping, and stiffness matrices of the 18-DOF full-order model. The error "spikes" in Figs. 3.2a through 3.2c are all very small and are due to the stiff elements that connect nodes 9 and 18 and nodes 10 and 17, respectively[1].

Identification of Reduced-Order Models

System identification tests of real structures are typically based on (sometimes triaxial) measurements taken at 25 to 500 nodes, whereas finite element models of the (infinite-DOF) structures are generally of the order of 1000 to 100,000 DOFs. In order to test the performance of the SSID Algorithm in identifying reduced-order models, simulated tests were performed on the "payload simulator" by eliminating the FRF test data at four nodes (2, 3, 6, 7), reducing the

---

[1]Multipoint constraints between DOFs 9 and 18 and DOFs 10 and 17 were later introduced to reduce the original 54-DOF FE model to a 52-DOF model.
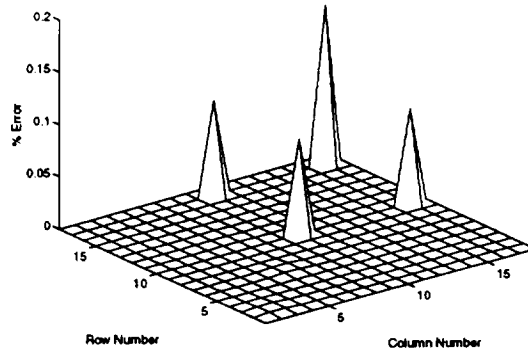
(a) Mass matrix error.
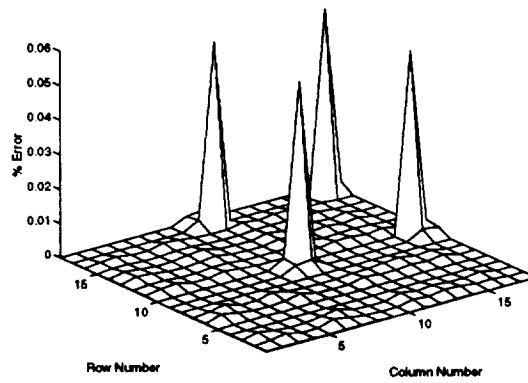
(b) Damping matrix error.
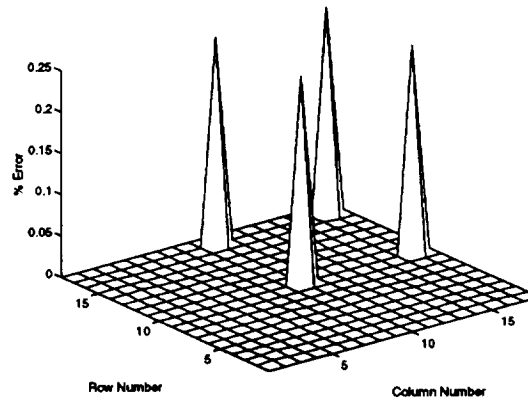
(c) Stiffness matrix error.

Figure 3.2: Percent errors in elements of the substructure matrices.

system from an 18-DOF system to a 14-DOF system.

The first reduced-order simulation was run without added measurement noise in order to examine the effect of spatial filtering of the data. The SSID identification was based on simulated FRF data generated at 1021 frequency lines equally spaced at 0.5 Hz between 2 Hz and 512 Hz. Since spatial filtering to obtain a reduced-order model introduces bias error in the data, the TLS method was used, even though there was no random "measurement noise" added for this case. Based on the SSID-identified 14-DOF reduced-order model, twelve of the fourteen undamped natural frequencies were identified to within 0.5%. Figure 3.3 shows a comparison of an exact driving-point FRF and the corresponding FRF based on the SSID-identified 14-DOF reduced-order model.

Next, in order to simulate actual test conditions, noise was added to produce "measured" FRFs for a simulated 14-DOF reduced-order test. Random noise was added to the magnitude and phase of the "measured" FRFs, with the amount of noise specified in terms of the maximum percentage of the RMS magnitude of each FRF and a maximum angle error on phase. Signal averaging was employed in these simulations, just as averaging would be employed in an actual test. The two least-squares methods, the ordinary least-squares (OLS) method and the total least-squares (TLS) method, were used to solve the two over-determined sets of equations, Eqs. 2.7 and 2.23.

Simulated FRF data was generated at 1021 frequency lines equally spaced at 0.5 Hz between 2 Hz and 512 Hz. For these simulations 3% amplitude noise and $3°$ phase noise was added to generate "measured" FRFs. These FRFs were averaged over $N = 100$ samples.
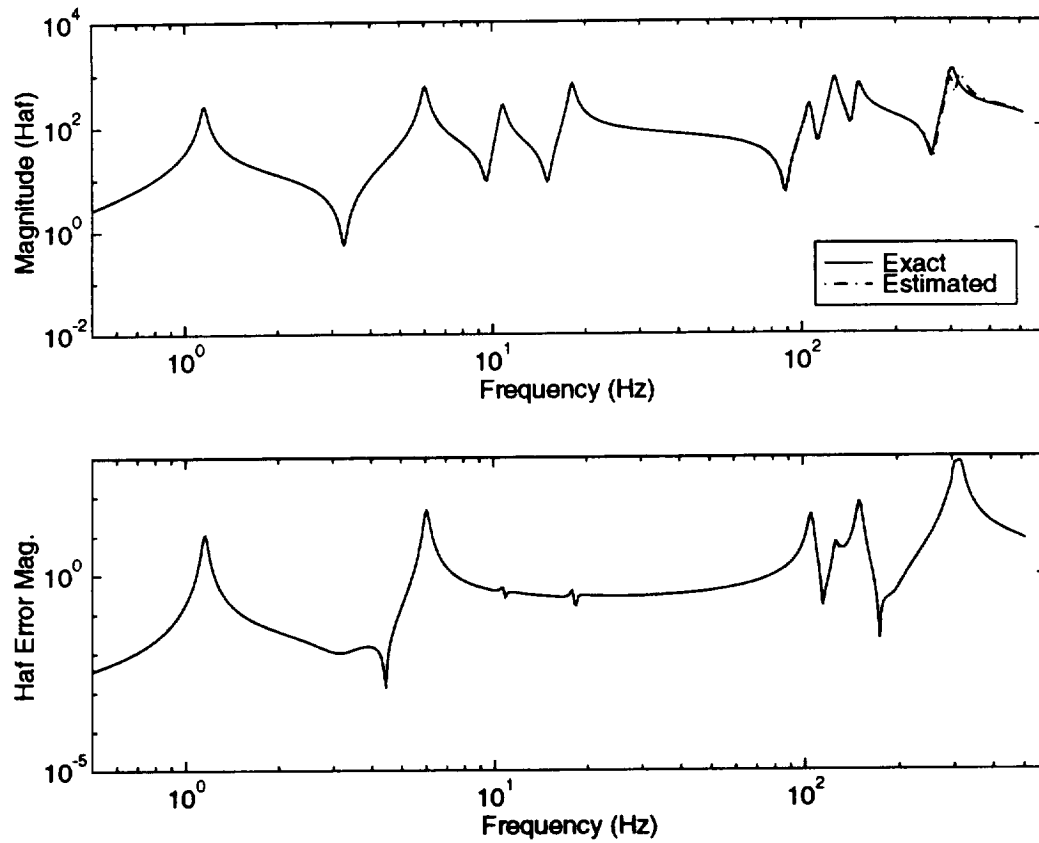
Figure 3.3: Exact driving-point FRF and FRF based on reduced-order SSID model (no noise).

In Table 3.1, the natural frequencies generated from the OLS- and TLS-estimated 14-DOF M and K matrices are compared to the first fourteen exact undamped natural frequencies of the full-order (18-DOF) system and to the SSID-identified undamped natural frequencies based on noise-free (NF) FRFs. Figure 3.4a shows a comparison between an exact driving-point FRF and the

Table 3.1: Natural frequencies (Hz) of 14-DOF reduced-order models

Mode	Exact	NF	% Err	OLS	% Err	TLS	% Err
1	1.1543	1.1564	0.18	1.1360	1.58	1.3771	19.30
2	6.0384	6.0489	0.17	6.0372	0.02	5.9258	1.86
3	10.783	10.783	0.00	10.791	0.07	10.728	0.51
4	18.127	18.127	0.00	17.932	1.07	18.121	0.03
5	106.08	106.38	0.28	101.42	4.40	106.02	0.06
6	127.27	127.27	0.00	119.54	6.07	126.76	0.40
7	129.38	129.49	0.08	126.22	2.44	129.19	0.15
8	151.52	151.90	0.25	152.23	0.05	151.60	0.05
9	299.12	299.14	0.01	—	—	272.08	9.04
10	304.16	319.93	5.18	—	—	300.57	1.18
11	604.31	602.88	0.24	—	—	—	—
12	606.90	606.21	0.11	—	—	—	—
13	1212.4	—	—	—	—	—	—
14	1214.0	—	—	—	—	—	—

corresponding FRF based on the OLS-identified reduced-order model. Figure 3.4b shows a comparison between an exact driving-point FRF and the corresponding FRF based on the TLS-identified reduced-order model. The mode-1 errors are due to the lack of data near the fundamental natural frequency.
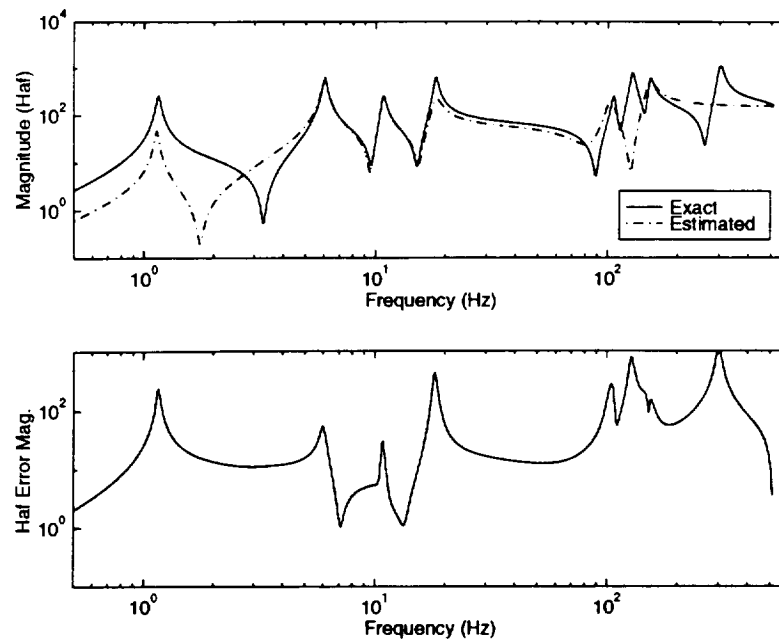
(a) Driving-point FRF based on 14-DOF OLS-identified model.
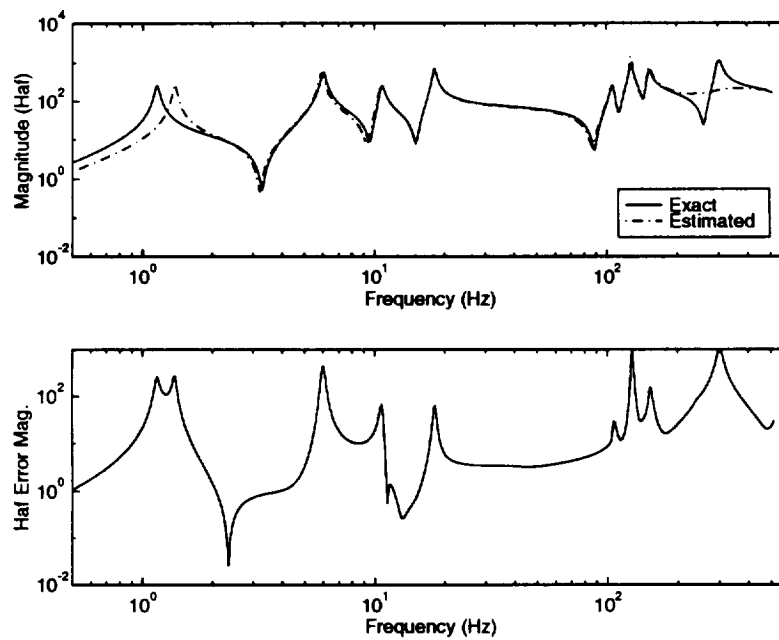
(b) Driving-point FRF based on 14-DOF TLS-identified model.

Figure 3.4: Frequency response functions for the 14-DOF simulated reduced-order vibration test.

3.2.3 Conclusions

The conclusions of this paper are:

- With simulated noise-free data, the SSID Algorithm exactly identified the 18-DOF full-order model and also did an excellent job identifying a 14-DOF reduced-order model.

- From simulated noisy data, the algorithm still identified acceptable reduced-order substructure system matrices. The TLS method proved to be better than the OLS method for handling the noisy data.

3.3 Frequency-Domain Substructure System Identification – (Ref. [3])

This paper, which is based on Ref. [1], first reviews the basic SSID theory (Chapt. 2 above) and the least-squares solution methods (Sect. 3.2.1 above). It then presents the step that is introduced into the SSID Algorithm to create pseudo degrees of freedom. Finally, simulation results on the following topics are presented: the relationship between model order and data bandwidth, the effectiveness of various least-squares methods in handling noisy data, and the use of pseudo degrees of freedom to expand the model order.

3.3.1 Model Order Determination; Pseudo Degrees of Freedom

Perhaps the most important, and most difficult, part of system identification is the determination of the proper model order. For structures with a very high modal density, there are typically more modes in the frequency

bandwidth than there are output sensors. For many system identification algorithms, including the SSID Algorithm, this poses a serious problem.

In the SSID formulation given in Chapt. 2, the model order is limited to the number of output sensors. This could be a serious drawback. For the case when there are more modes present than sensors, the size of the model must be expanded. An attempt to expand the size of the identification has been developed using *pseudo degrees of freedom*. The additional degrees of freedom are obtained by stacking the data used in Eq. 2.7 differently. The input frequency spectrum is divided in half, into a low-frequency spectrum and a high-frequency spectrum. In Eq. 2.9, the low-frequency response is then stacked on top of the high-frequency response as shown:

$$
\left[\frac{H_{af}}{jw} \right] \equiv
\begin{bmatrix}
\frac{1}{jw_1} H_{a_1 f_1}(\omega_1) & \cdots & \frac{1}{jw_{N_e}} H_{a_1 f_{N_f}}(\omega_{N_e}) \\
 & & \vdots \\
\frac{1}{jw_1} H_{a_{N_x} f_1}(\omega_1) & \cdots & \frac{1}{jw_{N_e}} H_{a_{N_x} f_{N_f}}(\omega_{N_e}) \\
\frac{1}{jw_{N_{e+1}}} H_{a_1 f_1}(\omega_{N_{e+1}}) & \cdots & \frac{1}{jw_{N_\omega}} H_{a_1 f_{N_f}}(\omega_{N_\omega}) \\
 & & \vdots \\
\frac{1}{jw_{N_{e+1}}} H_{a_{N_x} f_1}(\omega_{N_{e+1}}) & \cdots & \frac{1}{jw_{N_\omega}} H_{a_{N_x} f_{N_f}}(\omega_{N_\omega})
\end{bmatrix}
\tag{3.4}
$$

where $N_e = \frac{N_\omega}{2}$. Stacking the data in this manner essentially doubles the order of the model.

Although the lower partition of data is measured at the same physical coordinates as the upper partition of lower-frequency data, the system modes that contribute to the two sets of data are not identical. The lower partition is referred to as data from pseudo degrees of freedom. After Eq. 2.7 is solved using

the expanded model, the state-space eigenvalue problem, Eq. 2.12, is solved. However, the details of the second step of the algorithm, the identification of the system matrices (Eqs. 2.10 through 2.26), have yet to be resolved. Results obtained by processing through the first step of the SSID algorithm employing pseudo degrees of freedom are given below.

3.3.2 Numerical Simulation Results

The analytical model used in the simulations was the 52-DOF "payload simulator" FEM. The FEM consists of 18 nodes and 20 beam elements and is illustrated in Fig. 3.1. The payload simulator is supported by soft springs at nodes 11, 13, 14, and 16 to simulate a bungee cord suspension system. The three interface degrees of freedom for this structure are the Z-translational degrees of freedom at nodes 4, 8, and 18. To include the effects of damping in the system, modal damping at a level of 2% was added to all of the modes to obtain a physical damping matrix for the finite element model.

To generate the "experimental data" used in the simulations, the frequency response functions were generated by solving Eq. 2.6 for $A(\omega_k)$, given M, C, K, and $F(\omega_k)$ for the 52-DOF model. For the simulations presented in this paper, active excitation was used at all of the interface degrees of freedom; that is, no reaction forces were included. The input forcing function at each frequency ω_k consisted of three independent unit forces applied in the Z-translational direction at nodes 4, 8, and 18 respectively.

Reduced-Order Models

The simulations presented here demonstrate the ability of the SSID algorithm to predict the dynamic characteristics of a structure when only a limited number of output sensors is available. In a test environment, spatial truncation is inevitable, since it is impossible to measure the response of all of the degrees of freedom of a continuous structure. Three different reduced-order models were used in the simulations (10-DOF, 12-DOF and 16-DOF), and the respective DOFs were selected by using Kammer's Effective Independence method [15]. The modes of the resulting reduced-order models correspond to modes of the original system that are dominated by Z-translations.

Data Bandwidth Effects

For each of the reduced-order models, three different input frequency ranges were used to generate test data. This was done to determine how the SSID algorithm handles residual information. The identified model depends on the frequency range; for each model size, better results can be obtained by adjusting the frequency range until the best frequency range is found. In a test environment, the "best" frequency range is unknown, so three input frequency ranges were arbitrarily selected. The different frequency ranges are summarized in Table 3.2.

Estimated undamped natural frequencies and estimated damping factors were obtained for three different reduced-order models – 10-DOF, 12-DOF, and 16-DOF. Drive-point FRFs at node 4 were obtained for each of the three reduced-order models for the different input frequency ranges. Results are presented here only for the 12-DOF model. The estimated undamped natural

Table 3.2: Input Frequency Spectra

No.	Min. Freq. (Hz)	Max. Freq. (Hz)	No. Freq. Lines	Δf (Hz)
1	1	300	512	0.584
2	1	650	512	1.267
3	1	2100	1024	2.050

frequencies and damping factors of the 12-DOF model for the different input frequency ranges are listed in Tables 3.3 and 3.4. The corresponding FRFs are shown in Figure 3.5. For the 12-DOF model, the best results are obtained for the frequency ranges 1–300 Hz and 1–650 Hz. Note that the model corresponding to the input frequency range of 1–300 Hz was able to correctly estimate the system's response for modes 11 and 12 even though they are above the 300 Hz upper limit of the FRF data. The synthesized FRFs for these two models match very closely to those of the exact response, except near the response of the 12th mode. Here, the model corresponding to the first frequency range underestimates the response while the model corresponding to the 2nd input frequency range overestimates the magnitude of the response.

Table 3.3: Estimated Natural Frequencies — 12-DOF Model vs Input Frequency Spectrum

Exact Freq. (Hz)	Fmax=300 Hz		Fmax=650 Hz		Fmax=2100 Hz	
	Freq. (Hz)	Percent Error	Freq. (Hz)	Percent Error	Freq. (Hz)	Percent Error
1.1564	1.1564	1.465e–03	1.1563	1.560e–02	1.1577	1.073e–01
6.0642	6.0642	3.454e–05	6.0643	6.787e–04	6.0620	3.767e–02
10.783	10.783	8.332e–06	10.783	2.530e–03	10.785	1.427e–02
18.127	18.127	1.780e–06	18.127	2.632e–03	18.112	7.970e–02
109.49	109.49	5.694e–04	109.49	2.860e–03	109.54	4.366e–02
127.14	127.14	1.377e–04	127.19	4.276e–02	127.30	1.261e–01
137.82	137.82	7.153e–05	137.82	7.165e–04	137.83	5.248e–03
156.87	156.86	8.364e–05	156.86	7.596e–03	156.87	4.080e–03
297.66	296.64	6.828e–03	296.99	2.239e–01	299.29	5.461e–01
304.47	304.58	3.859e–02	304.41	1.833e–02	305.56	3.598e–01
606.45	602.08	7.211e–01	605.93	8.683e–02	616.79	1.704e+00
631.08	614.86	2.570e+00	609.92	3.353e+00	643.57	1.979e+00

Table 3.4: Estimated Damping Factors — 12-DOF Model vs Input Freq. Spectrum (Exact Damp. Ratio = 0.02)

| Fmax=300 Hz		Fmax=650 Hz		Fmax=2100 Hz	
Damp. Ratio	Percent Error	Damp. Ratio	Percent Error	Damp. Ratio	Percent Error
0.02000	9.909e–03	0.02006	2.965e–01	0.01782	1.088e+01
0.02000	2.023e–03	0.01995	2.550e–01	0.01854	7.309e+00
0.02000	4.948e–03	0.02025	1.257e+00	0.01558	2.209e+01
0.02000	9.197e–04	0.01936	3.193e+00	0.01929	3.524e+00
0.02000	1.234e–02	0.02003	1.563e–01	0.01985	7.721e–01
0.02000	6.847e–03	0.02012	6.068e–01	0.01855	7.255e+00
0.02000	1.396e–03	0.01999	4.555e–02	0.01982	8.789e–01
0.02000	5.182e–03	0.02000	4.095e–03	0.02000	5.835e–03
0.01999	7.062e–02	0.01982	8.829e–01	0.03171	5.855e+01
0.02004	2.125e–01	0.01989	5.649e–01	0.02753	3.764e+01
0.02003	1.565e–01	0.01979	1.029e+00	0.01807	9.641e+00
0.02003	1.735e–01	0.02774	3.869e+01	0.02286	1.432e+01
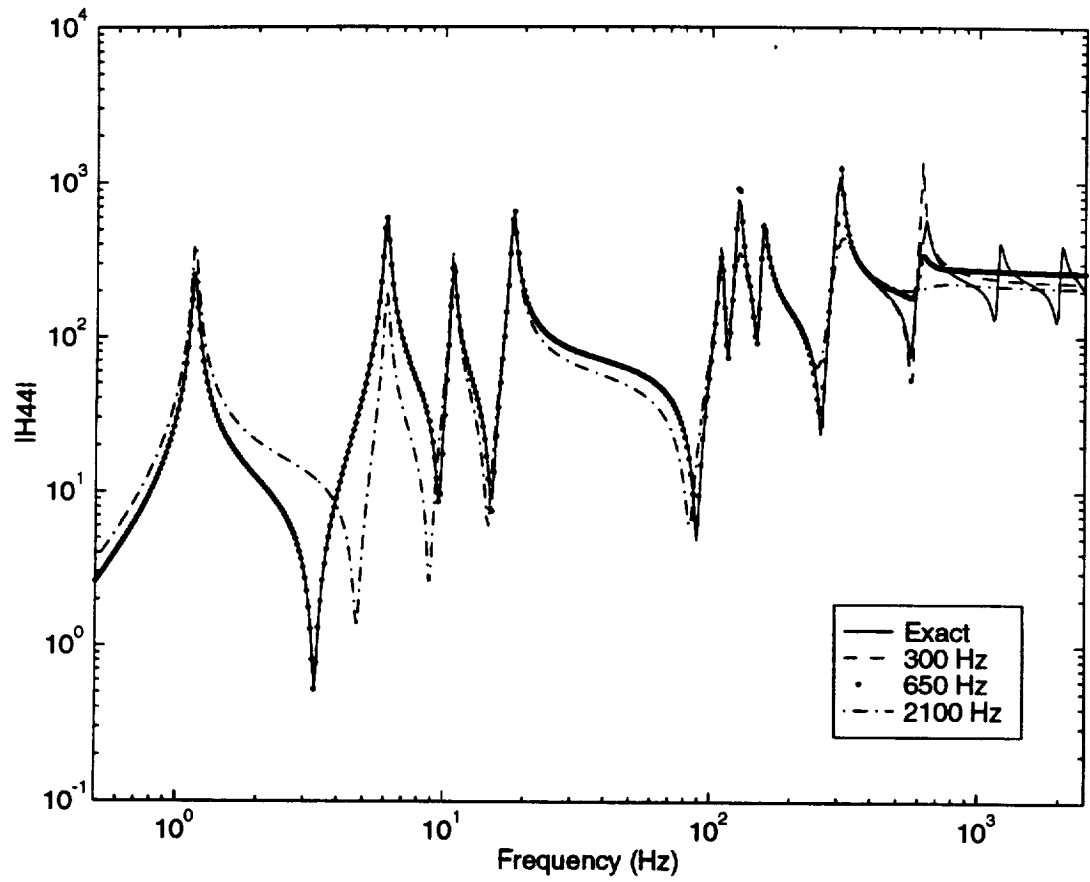
Figure 3.5: Comparison of FRFs for the 12-DOF Model vs Input Frequency Spectrum

Effect of Noise

Noise was added to the data to represent the errors inherent with actual test data, such as transducer error, signal processing and conditioning error. or other errors and uncertainties present in the measurement process. The noise added to the simulated FRF data was uniformly distributed, pure random, and zero mean. A noise level of 2% was used in the simulations in this study. The noise level is the percent of the root-mean-square (RMS) value of the random noise to the RMS value of the noise-free signal. Acceleration is usually measured as the output of the structure, so the magnitude of the noise is proportional to the magnitude of each accelerance FRF spectrum, not the receptance frequency response. A random phase error was also introduced; the maximum error on the phase was 2°. To reduce the effect of the noise, signal averaging was used, just as averaging would be employed in an actual test. The measured FRFs were averaged over 40 samples.

The three least-squares methods discussed in Ref. [1] – ordinary least squares (OLS), total least squares (TLS), and scaled total least squares (STLS) – were used to solve the over-determined system of equations, Eq. 2.7. No acceptable solution for any of the reduced-order models was ever obtained using the OLS method. The resulting identified system matrices were not positive definite, and typically yielded complex estimates for the undamped natural frequencies. Increasing the number of averages did not significantly improve the resulting solution. Thus, for implementation of the SSID algorithm in test environments, a TLS solver will be necessary.

Comparisons of the results for the 12-DOF model are shown in Fig. 3.6

and in Tables 3.5 and 3.6. The STLS method provides a slightly better esti-
mation of the dynamic characteristics of the original structure than the TLS
solution for the low-frequency response. Both solutions overestimate the re-
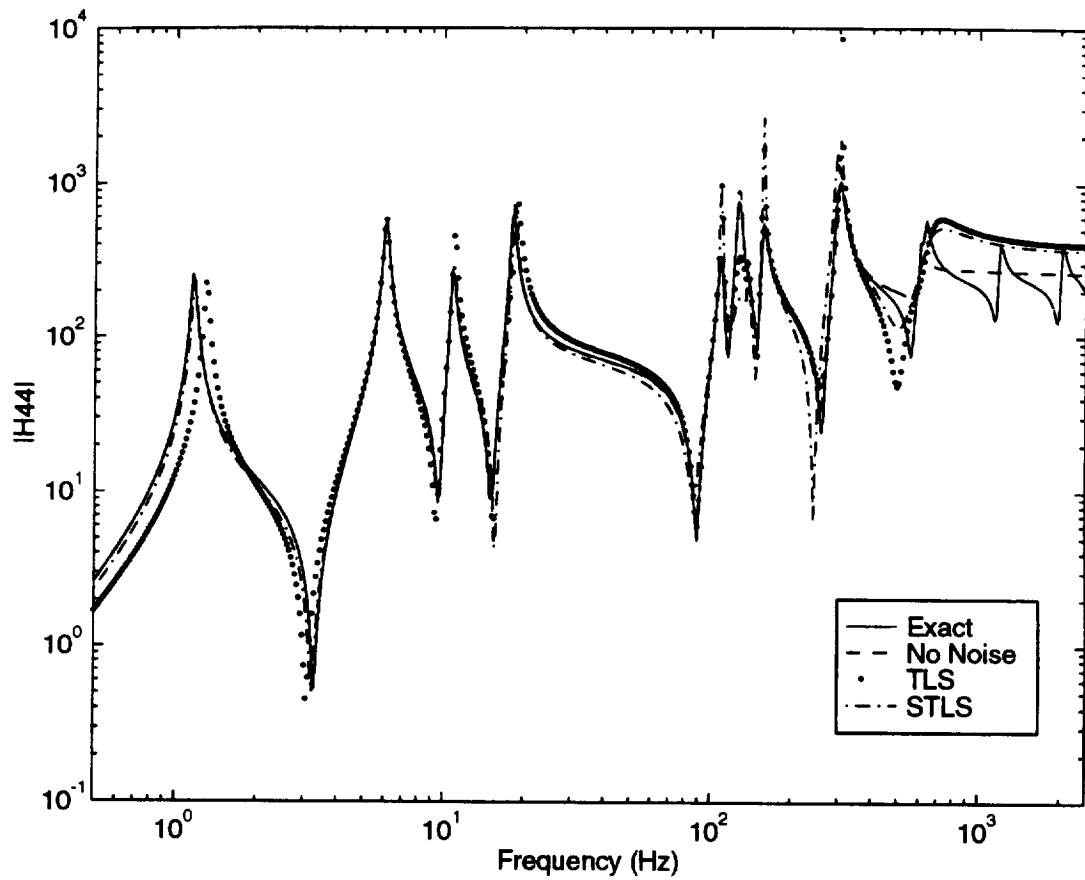sponse of the structure for frequencies greater than the input frequency range
of 1–650 Hz.

Figure 3.6: Comparison of FRFs of 12-DOF Model vs Solution Method

Table 3.5: Estimated Natural Frequencies — 12-DOF Model vs Solution Method

Exact	Noise Free		TLS		STLS	
Freq. (Hz)	Freq. (Hz)	Percent Error	Freq. (Hz)	Percent Error	Freq. (Hz)	Percent Error
1.1564	1.1563	1.560e–02	1.2983	1.226e+01	1.1701	1.182e+00
6.0642	6.0643	6.787e–04	6.0660	2.812e–02	605.85	9.405e–02
10.783	10.783	2.530e–03	10.957	1.605e+00	10.830	4.323e–01
18.127	18.127	2.632e–03	18.761	3.500e+00	18.221	5.221e–01
109.49	109.49	2.860e–03	109.43	5.631e–02	109.46	2.827e–02
127.14	127.19	4.276e–02	127.61	3.710e–01	127.49	2.772e–01
137.82	137.82	7.165e–04	137.70	8.719e–02	137.73	6.834e–02
156.87	156.86	7.596e–03	156.66	1.359e–01	156.71	1.057e–01
297.66	296.99	2.239e–01	291.23	2.160e+00	295.51	7.223e–01
304.47	304.41	1.833e–02	304.49	6.377e–03	304.96	1.610e–01
606.45	605.93	8.683e–02	600.29	1.016e+00	603.69	4.558e–01
631.08	609.92	3.353e+00	653.34	3.528e+00	654.15	3.656e+00

Table 3.6: Estimated Damping Factors — 12-DOF Model vs Solution Method (Exact Damp. Ratio = 0.02)

Noise Free		TLS		STLS	
Damp. Ratio	Percent Error	Damp. Ratio	Percent Error	Damp. Ratio	Percent Error
0.02006	2.965e–01	0.01737	1.312e+01	0.02002	9.185e–02
0.01995	2.550e–01	0.01975	1.225e+00	0.01989	5.410e–01
0.02025	1.257e+00	0.02139	6.977e+00	0.02225	1.127e+01
0.01936	3.193e+00	0.01758	1.211e+01	0.01717	1.413e+01
0.02003	1.563e–01	0.02158	7.932e+00	0.02105	5.268e+00
0.02012	6.068e–01	0.01935	3.234e+00	0.01856	7.178e+00
0.01999	4.555e–02	0.02171	8.545e+00	0.02154	7.699e+00
0.02000	4.095e–03	0.02102	5.094e+00	0.02089	4.474e+00
0.01982	8.829e–01	0.02975	4.876e+01	0.02880	4.400e+01
0.01989	5.649e–01	0.02251	1.254e+01	0.02257	1.285e+01
0.01979	1.029e+00	0.02351	1.754e+01	0.01557	2.215e+01
0.02774	3.869e+01	0.06257	2.128e+02	0.06822	2.411e+02

Pseudo Degrees of Freedom

This section presents the results of augmenting the model order using pseudo degrees of freedom (PDF). For this simulation, the 10-DOF model was used and the the input frequency range was 1–2100 Hz with 1024 equally spaced frequency lines. Using the pseudo degrees of freedom, the model order was expanded to create a 20-DOF pseudo-degree-of-freedom model, and the identification process through Eq. 2.12 was completed; the remaining portion of the identification procedure has yet to be defined for pseudo degrees of freedom. No noise was added to the data. Table 3.7 gives a listing of the estimated frequencies from the solution of Eq. 2.12 and compares those to the frequencies obtained using only the original ten degrees of freedom.

Table 3.7: Identified Natural Frequencies Using Pseudo Degrees of Freedom

Pseudo DOF Model				Original Model	
Mode No.	Freq. (Hz)	Mode No.	Freq. (Hz)	Mode No.	Freq. (Hz)
1	1.1026	11	304.24	1	1.1454
2	6.0572	12	463.91	2	6.0878
3	10.387	13	497.10	3	10.989
4	18.063	14	1189.8	4	18.293
5	109.50	15	1193.2	5	109.52
6	128.19	16	1675.1	6	127.75
7	137.82	17	1686.4	7	137.81
8	156.89	18	1713.0	8	156.99
9	271.10	19	2029.5	9	308.15
10	297.17	20	2031.6	10	311.36

Using the original 10 degrees of freedom, only the lowest 10 modes could be identified even though more are present in the data. When the order of

the model was expanded by use of pseudo degrees of freedom, the model was able to identify 4 additional target modes, modes 21, 22, 29, and 30, plus some additional computational modes. Some sort of modal quality indicator is needed to distinguish between the physical and computational modes of the PDF model. This approach doubles the model order. In some instances, this may be too large and the model order may need to be decreased from twice the original size. A reduction step would then be required to determine the appropriate model order. The initial results are encouraging, since some of the higher frequencies can be identified using the pseudo degrees of freedom.

3.3.3 Conclusions

The conclusions reached in this paper are:

- Accurate reduced-order models can be identified by use of the SSID Algorithm with the total least-squares method used to solve the overdetermined systems of linear equations.

- Pseudo degrees of freedom can be introduced to expand the number of degrees of freedom of the model beyond the number of output sensors for which measured response data is available. However, further research is needed on this topic.

3.4 A Craig-Bampton Test-Analysis Model – (Ref. [4])

To verify that a finite element model (FEM) of a structure is sufficiently accurate to predict the structure's response, the FEM must be test validated.

The accuracy of the FEM is often assessed by comparing the modal parameters of the analytical model to those extracted using vibration test data. Test and analysis natural frequencies can be compared directly. However, the modal vectors cannot be readily compared since the FEM will have many more DOFs than the test configuration will have accelerometers. In order to compare the FEM results with the test results, a reduced-order representation of the FEM called a *test-analysis model* (TAM) is usually created. This leads to a one-to-one relationship between the TAM DOFs and the number of accelerometers in the test configuration. Numerous procedures for generating reduced-order models have been developed. The simplest and most straightforward reduction procedure is the Guyan, or static, reduction method [16]. This method is very useful for generating test-analysis models since the measured DOFs can be selected as the ones to be retained in the reduction process. However, the Guyan reduction method is quite sensitive to the selection of omitted DOFs and often results in poor accuracy if there is inertia associated with the omitted degrees of freedom.

References [1] and [17] describe an extension of the Craig-Bampton component mode synthesis method that can be used to create a TAM for modal survey test-analysis correlation. In the original Craig-Bampton formulation, the model coordinates are a combination of physical coordinates and generalized coordinates. In the proposed test-analysis model (TAM), the accuracy of the original Craig-Bampton formulation is retained, but the TAM is referred to the test physical coordinates only. A systematic procedure is presented to identify the fixed-interface normal modes that contribute most to the retained physical DOFs. This method is particularly useful when the target modes

are not the lowest consecutive modes of the system. The performance of the proposed method is compared to the performance of two other popular model-reduction techniques.

3.4.1 Craig-Bampton Models in Generalized Coordinates

The N physical degrees of freedom of the substructure are first partitioned into two sets – the boundary, or interface, DOFs and the interior DOFs:

$$x = \left\{ \begin{array}{c} x_i \\ x_b \end{array} \right\}$$ (3.5)

where x_b are the boundary degrees of freedom and x_i are the interior degrees of freedom[2]. With damping omitted, the equations of motion are

$$\left[\begin{array}{cc} M_{ii} & M_{ib} \\ M_{bi} & M_{bb} \end{array} \right] \left\{ \begin{array}{c} \ddot{x}_i \\ \ddot{x}_b \end{array} \right\} + \left[\begin{array}{cc} K_{ii} & K_{ib} \\ K_{bi} & K_{bb} \end{array} \right] \left\{ \begin{array}{c} x_i \\ x_b \end{array} \right\} = \left\{ \begin{array}{c} f_i \\ f_b \end{array} \right\}$$ (3.6)

The Craig-Bampton method uses the Ritz transformation

$$x = T_{CB_1} q$$ (3.7)

where

$$T_{CB_1} = \left[\begin{array}{cc} \Phi_n & \Psi_c \\ 0 & I \end{array} \right]$$ (3.8)

$$\Psi_c = -K_{ii}^{-1} K_{ib}$$ (3.9)

and q is a vector of generalized coordinates having the form

$$q = \left\{ \begin{array}{c} q_i \\ x_b \end{array} \right\}$$ (3.10)

---

[2]Although originally developed as a component mode synthesis method, the method can be considered to be a general model-reduction method by simply letting $\underline{i} \rightarrow \underline{o}$ and $\underline{b} \rightarrow \underline{a}$. That is, let "interior" coordinates be more general "omitted" DOFs and, likewise, let "boundary" coordinates be more general "active" coordinates.

The first column-partition of the Craig-Bampton transformation matrix contains the fixed-interface normal modes. This describes the motion of the interior DOFs relative to the boundary DOFs in terms of the normal modes of the substructure with the boundary DOFs fixed. The fixed-interface normal modes are obtained by solving the eigenproblem for the interior DOFs

$$(K_{ii} - \omega_r^2 M_{ii})\phi_r = 0 \tag{3.11}$$

or

$$K_{ii}\Phi_n = M_{ii}\Phi_n\Lambda_n \tag{3.12}$$

where the subscript r denotes the rth fixed-interface normal mode. The second column-partition of the transformation matrix contains the constraint modes. The rth constraint mode is defined by producing a unit displacement at the rth boundary degree of freedom with all other boundary DOFs constrained and with all interior DOFs unconstrained.

The final reduced-order matrices obtained are based on a combination of physical (boundary) coordinates and generalized modal coordinates. These generalized coordinates cannot be used directly for test-analysis correlation and therefore must be transformed into suitable physical coordinates.

3.4.2 Craig-Bampton Models in Physical Coordinates

The transformation from generalized coordinates to physical coordinates for Craig-Bampton models is described by Huang and Craig [17]. The interior physical DOFs are partitioned via

$$\{x_i\} = \left\{ \begin{array}{c} x_r \\ x_o \end{array} \right\} \tag{3.13}$$

where x_r are the retained DOFs where measurements will be made during the vibration test, and x_o are the omitted DOFs. The equations of motion can be rewritten as

$$\begin{bmatrix} M_{rr} & M_{ro} & M_{rb} \\ M_{or} & M_{oo} & M_{ob} \\ M_{br} & M_{bo} & M_{bb} \end{bmatrix} \begin{Bmatrix} \ddot{x}_r \\ \ddot{x}_o \\ \ddot{x}_b \end{Bmatrix} + \begin{bmatrix} K_{rr} & K_{ro} & K_{rb} \\ K_{or} & K_{oo} & K_{ob} \\ K_{br} & K_{bo} & K_{bb} \end{bmatrix} \begin{Bmatrix} x_r \\ x_o \\ x_b \end{Bmatrix} = \begin{Bmatrix} f_r \\ f_o \\ f_b \end{Bmatrix} \quad (3.14)$$

Then, Eq. 3.7 can be written as

$$\begin{Bmatrix} x_r \\ x_o \\ x_b \end{Bmatrix} = T_{CB_1} q = \begin{bmatrix} \Phi_r & \Psi_r \\ \Phi_o & \Psi_o \\ 0 & I \end{bmatrix} \begin{Bmatrix} q_i \\ x_b \end{Bmatrix} \quad (3.15)$$

This leads to the transformation matrix T_{CB_2} relating the generalized coordinates to physical coordinates to be used during the test:

$$T_{CB_2} = \begin{bmatrix} (\Phi_{nr}^T \Phi_{nr})^{-1} \Phi_{nr}^T & -(\Phi_{nr}^T \Phi_{nr})^{-1} \Psi_{cr}^T \\ 0 & I \end{bmatrix} \quad (3.16)$$

A similar approach was developed by Kammer [18], but Huang and Craig point out that the contribution of the constraint modes to the transformation matrix T_{CB_2} was not included in Kammer's formulation of the transformation.

The order of the Craig-Bampton model is determined by how many fixed-interface normal modes are used to augment the constraint modes when forming the transformation matrices. If the desired size of the reduced-order model is k, then the number of fixed-interface normal modes retained is $n_m = k - n_b$. Typically, only the lowest n_m fixed-interface normal modes are kept. This results in a Craig-Bampton model that accurately predicts the lowest k modes of the substructure. However, if the target modes are not the lowest consecutive modes, then the analytical modes from the Craig-Bampton model will not necessarily correlate well with the target test modes.

3.4.3 Selection of Component Modes

In order for the Craig-Bampton model to represent the target modes, a proper set of fixed-interface normal modes must be selected. This set consists of the fixed-interface normal modes that contribute most to the target modes. The selection process is accomplished in the same manner that was used in Ref. [19] to determine which coordinates to select as the rigid-body coordinates to solve a semidefinite eigenvalue problem. Gaussian elimination or other factorization methods can be performed on Φ_{nr} with pivot selection being used to determine which columns of Φ_{nr} contribute most to the target modes. Full column and row pivoting is necessary in the event that one of the retained interior DOFs lies along a node line of a fixed-interface normal mode. It was observed, however, that this selection technique was dependent upon the scaling of the fixed-interface normal modes, so further study is needed to remove the scaling dependence.

A Craig-Bampton test-analysis model suitable for correlation with the test modes can be obtained by choosing the fixed-interface normal modes that contribute most to the test modes. The final form of the transformations defining the Craig-Bampton TAM are given by

$$M_{CB} = T_{CB_2}^T T_{CB_1}^T M T_{CB_1} T_{CB_2} \qquad (3.17)$$

$$K_{CB} = T_{CB_2}^T T_{CB_1}^T K T_{CB_1} T_{CB_2} \qquad (3.18)$$

$$f_{CB} = T_{CB_2}^T T_{CB_1}^T f \qquad (3.19)$$

where the transformation matrices contain the proper set of fixed-interface normal modes.

3.4.4 Simulation Results

The analytical model used in the simulations is a 52-DOF FEM of the "Payload Simulator" in the Structural Dynamics Laboratory at The University of Texas at Austin. The physical structure consists of two 60-in.-long aluminum box beams connected by two 20-in. cross-beams at either end. The FEM consists of 18 nodes and 20 beam elements and is illustrated in Fig. 3.1.

The physical structure undergoes motion primarily in the Z direction, so all of the X and Y translations and Z rotations are constrained in the finite element model. The payload simulator is supported by soft springs at nodes 11, 13, 14, and 16 to simulate a bungee cord suspension system. The modes of interest for this structure are the 3 rigid-body modes (modes 1-3), the fundamental torsion mode (mode 4), and the primary bending modes (modes 5-10, 17, 18, 21, 22, 29, and 30). These are the modes that are dominated by translational motion in the Z-direction. Note that the target modes are not the lowest consecutive modes of the structure, but are distributed throughout the modal spectrum.

The Craig-Bampton reduced-order model in physical coordinates is compared to two other TAM models, the Guyan model and the Improved Reduction System (IRS) model. The appropriate fixed-interface normal modes for use in the Craig-Bampton models were selected using the technique described in Sect. 3.4.3. The estimated natural frequencies and the predicted dynamic response are compared for 16-DOF reduced-order models based on the three TAMs. Cross-orthogonality checks were also performed for each TAM.
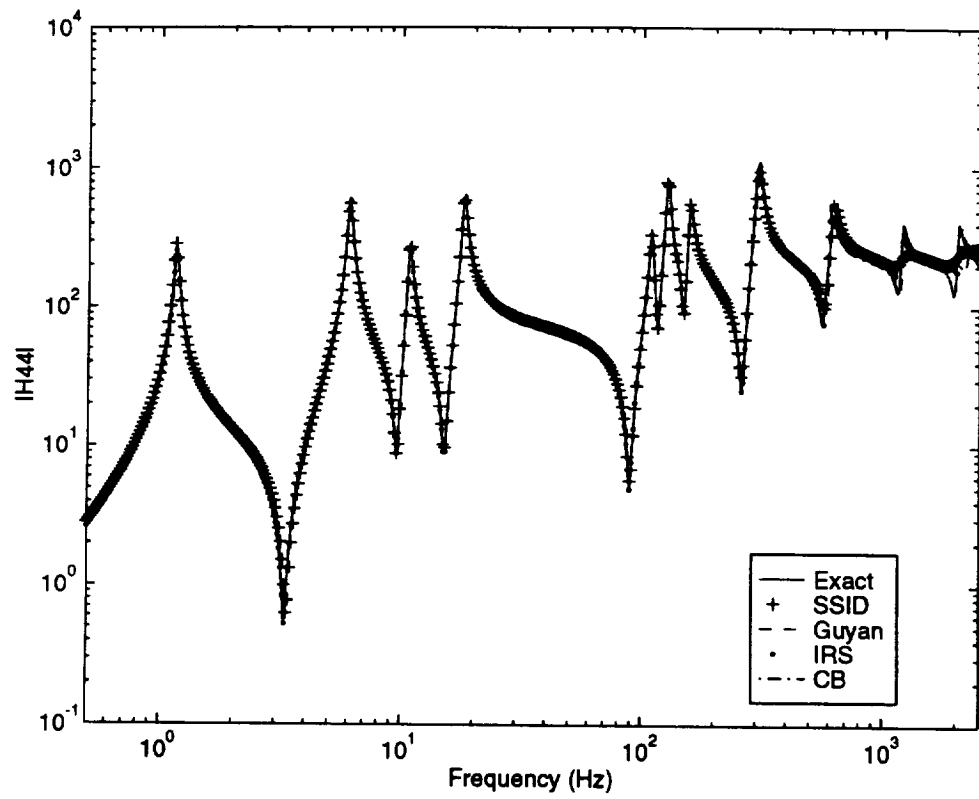
Figure 3.7: Comparison of FRFs for 16-DOF TAMs

Table 3.8: Estimated Natural Frequencies — 16-DOF TAMs

SSID		Guyan		IRS		C-B	
Freq. (Hz)	Percent Error	Freq. (Hz)	Percent Error	Freq. (Hz)	Percent Error	Freq. (Hz)	Percent Error
1.1507	4.948e–01	1.1564	1.864e–06	1.1564	3.904e–08	1.1564	1.242e–07
6.0628	2.430e–02	6.0643	7.634e–05	6.0642	1.108e–09	6.0642	5.057e–06
10.807	2.165e–01	10.783	3.467e–01	10.783	7.736e–10	10.783	2.255e–04
18.115	6.439e–02	18.127	2.036e–03	18.127	1.557e–09	18.127	1.569e–03
109.49	1.539e–03	109.50	8.567e–03	109.49	5.435e–06	109.49	1.934e–03
127.15	7.669e–03	127.27	1.026e–01	127.14	1.943e–04	127.27	1.006e–01
137.82	2.866e–03	137.83	7.427e–03	137.82	6.314e–07	137.83	3.774e–03
156.86	5.341e–03	156.91	2.329e–02	156.87	2.836e–05	156.88	5.222e–03
297.61	1.796e–02	299.12	4.909e–01	297.75	3.140e–02	299.38	5.779e–01
304.41	1.745e–02	304.53	2.095e–02	304.47	6.180e–06	304.51	1.448e–02
606.24	3.595e–02	604.31	3.535e–01	595.50	1.807e+00	606.61	2.544e–02
626.89	6.648e–01	607.01	3.814e+00	606.43	3.906e+00	617.20	2.200e+00
1189.4	8.538e–02	1212.4	1.848e+00	1133.1	4.816e+00	1189.5	7.938e–02
1192.3	8.922e–02	1214.1	1.738e+00	1190.8	2.093e–01	1191.1	1.911e–01
2017.0	5.990e–01	2227.5	9.774e+00	1752.9	1.361e+01	2029.3	7.551e–03
2017.6	6.686e–01	2228.7	9.721e+00	2052.1	1.026e+00	2035.0	1.865e–01

Table 3.8 lists the estimated undamped natural frequencies for each of the reduced-order models. As expected, the Craig-Bampton and IRS models provide better estimations of the undamped natural frequencies than does the Guyan model. Overall, the frequencies are estimated best by the Craig-Bampton model. The table also shows the estimated undamped natural frequencies for a reduced-order model obtained by applying the SSID substructure system identification method with simulated FRFs for the 52-DOF FEM.

A comparison of the estimated FRFs for each of the 16-DOF reduced-order models is given in Fig. 3.7. The physical damping matrix used for each of the TAMs was computed by using the real normal modes estimated by each model, specifying a modal damping factor of 2% in each mode, and computing a modal damping matrix. As shown in Fig. 3.7, all three methods represent

the dynamic response of the original 52-DOF model very well.

3.4.5 Conclusions

The conclusions reached in this paper are:

- Although the Craig-Bampton model-reduction method was not originally developed for use as a test-analysis model reduction method, the results presented in this paper show that it can be used as such. A reduced-order model can be generated that has the accuracy of the Craig-Bampton method and also has the convenience of having all of the degrees of freedom in physical coordinates, making it suitable for correlation with test data.

- The process described in this paper for selecting the appropriate fixed-interface normal modes seems to be dependent upon the scaling of the modes. Further research is needed to determine an absolute measure that can be used to determine the fixed-interface normal modes that contribute most to the target modes.

3.5   A Band-Processing Algorithm for Structural System Identification − (Ref. [5])

This paper, which is based on Sects. 5.2 and 6.3 of Ref. [1], presents a band-processing algorithm for frequency-domain structural system identification. It describes a systematic procedure for using frequency response functions that are processed in overlapping frequency bands and then combined to create

a global system model of the test structure. A linear, viscous-damped, reduced-order system model $(M, C,$ and $K)$ is obtained. Numerical simulations illustrate the algorithm's ability to identify valid reduced-order structural models. The proposed algorithm promises to be a suitable candidate for implementation on parallel-processing computers.

Following a review of the basic SSID Algorithm, the revisions added to the basic algorithm to permit data to be processed in a sequence of overlapping frequency bands is presented. A flow chart of the expanded algorithm is given, and a simulation study is then presented in which the expanded algorithm is used to reduce the 52-DOF "payload simulator" FEM to a 16-DOF reduced-order model.

3.5.1 A Narrow-Band FRF Data-Processing Algorithm

Previous authors (e.g., Ref. [20]) have noted that frequency-domain identification algorithms generally result in better estimations when used as narrow-band identification procedures. However, sometimes not all of the target modes lie within a narrow frequency band. For instance, the target modes may span a frequency range of 2 kHz or more. Terms in the resulting frequency-domain equations of motion would vary by a minimum of eight orders in magnitude, and this could lead to the data being ill-conditioned. In the SSID algorithm, the first estimation step, (i.e., the solution of Eq. 2.7) is more prone to ill-conditioning than is the second step (i.e., the solution of Eq. 2.23), since the former step uses accelerance, mobility, and receptance frequency response functions.

In the basic formulation of the SSID algorithm (Chapt. 2) all of the measured data is to be processed simultaneously. As just pointed out, this could lead to numerical difficulties. To alleviate this problem, a concept referred to as *band processing* is introduced in this paper. The basic idea behind band processing is to work with narrow bands of frequency data individually, and thus avoid some of the conditioning problems. In this manner, experimental data spanning several decades can be processed incrementally, for example, 500 Hz at a time, by the SSID algorithm until all of the data has been included in the identified model.

The band processing is implemented in the SSID algorithm as follows. First, the experimental data is acquired in the usual manner covering as many decades as necessary to obtain all of the desired modes. The data is then divided into suitable bandwidths of overlapping frequency bands. Then the SSID algorithm is used to process each frequency band individually through the solution of the state-space eigenvalue problem, Eq. 2.12. From each complex-conjugate pair of eigenvalues, a natural frequency and damping factor can be computed:

$$\zeta_r = \frac{-\Re(\hat{\lambda}_r)}{|\hat{\lambda}_r|} \qquad r = 1, \ldots, N_x \tag{3.20}$$

$$\omega_r = \frac{\Im(\hat{\lambda}_r)}{\sqrt{1 - \zeta_r^2}} \qquad r = 1, \ldots, N_x \tag{3.21}$$

This step is repeated until all of the frequency bands have been processed.

The next step is to separate the structural roots from the computational roots, or "noise roots." In this study, four criteria were used to distinguish between the physical modes and computational modes.

1. To graphically aid in the selection process, the estimated natural frequencies and the frequency bands are plotted versus frequency over the entire frequency range. Any estimated frequencies lying outside of the given frequency band are discarded.

2. Roots with negative damping values are discarded.

3. The *modal phase collinearity* (MPC) is computed for each complex-conjugate pair of mode shapes.[6] Those modes with less than a specified MPC value are discarded. The value is dependent upon the level of noise in the measurement signal and the quality of the data.

4. If the root is not repeated in another frequency band, it is discarded. Thus, the need for the overlapping frequency bands. True structural roots will be estimated in multiple frequency bands, while computational ones are highly unlikely to be repeated in multiple frequency bands.

The flow chart in Fig. 3.8, which summarizes the steps in this band-processing procedure, is also provided in Refs. [1] and [5].

Once the computational roots are eliminated and the physical roots stored, the SSID algorithm can proceed to identify the system matrices just as before[3]. Any one of a set of repeated roots and corresponding eigenvectors can be arbitrarily selected from any frequency band for use in the second part of

---

[3]Previous works, e.g., Ref. [20], have carried out narrow-band frequency-domain identification of frequencies, damping factors, and mode shapes using the steps up to this point in the present algorithm. The remaining steps of the present band-processing algorithm have apparently not been considered by previous authors.
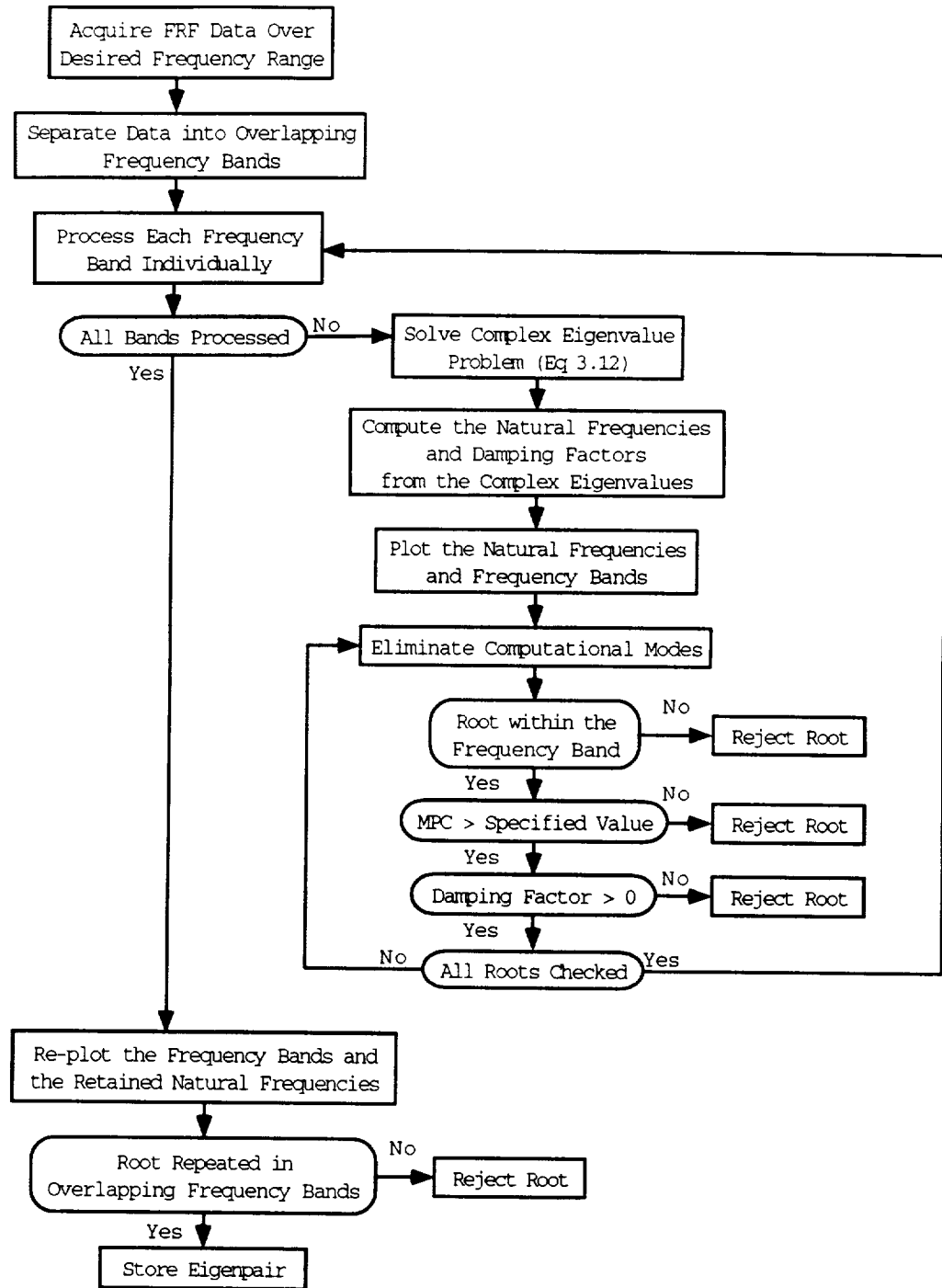
Figure 3.8: Flow Chart for Band Processing of FRF Data

the SSID algorithm since the eigenvectors are arbitrarily scaled. The scaling used to determine the final system matrices arises from the solution for the $\tilde{a}$ coefficients in Eq. 2.23.

In the band-processing simulations included in this paper, three different approaches where used to estimate the $\tilde{a}_r$ values. The first was to solve Eq. 2.23 and estimate the $\tilde{a}$ coefficients using all of the FRF data in the particular frequency band from which the root was selected. This approach is referred to as BP1. The second approach is similar to the first, except that only data near each particular resonance frequency is used in the estimation of the corresponding $\tilde{a}_r$ value. This approach is referred to as BP2. The third approach is to use the data obtained near the resonances of all of the selected roots simultaneously in Eq. 2.23; this is referred to as BP3. The first two approaches provide *local* estimations, while the last is a *global* one since data from multiple frequency bands is used simultaneously.

3.5.2 Simulation Results

This section presents the results of simulations where the band-processing approach described in the previous section was used in the identification procedure. Development of the band-processing approach was motivated by the unsuccessful identification of a particular 16-DOF model from noisy data. First, the band-processing method was applied to the 16-DOF model using noise-free data to determine if the idea would yield valid results. Then, simulated data containing noise was used.

Simulated FRF data for a 16-DOF model, with 1024 equally spaced fre-

quency lines over an input frequency spectrum of 1–2100 Hz, was used to test the proposed band-processing algorithm. To illustrate the procedure outlined in the previous section, the FRF data was divided into 100-Hz frequency bands with 50-Hz overlap, resulting in 41 frequency bands. For each frequency band, identified by the dark horizontal lines in Fig. 3.9, the SSID identification proceeded through the solution of Eq. 2.12. The estimated natural frequencies computed using Eq. 3.21 are plotted as $\times$'s in Fig. 3.9. The vertical lines indicate the target-mode frequencies. Note that even though each frequency band spans only 100 Hz, numerous target frequencies outside of a given band are also correctly identified. This only occurs when noise-free data is used. In addition, a number of "noise modes" are also identified. Following the band-processing flow chart, the roots in bands 1, 3, 6, 13, 24, and 40 were selected as the identified structural-mode parameters, and the remaining steps of the SSID algorithm were then carried out to identify the system matrices.

The three different approaches described in Section 3.5.1 for solving Eq. 2.23 were used to solve for the scale factors $\tilde{a}$. These approaches are referred to as BP1, BP2, and BP3 respectively. The BP1 estimates did not yield positive definite system matrices and are not included here. The results from the other two methods are shown in Tables 3.9 and 3.10 and in Fig. 3.10. The BP2 estimate provides the best estimation of the natural frequencies. However, the BP2 results tend to overestimate the response at high frequencies, while the response of BP3 is much closer to the one obtained using the original SSID formulation. The estimates of the damping factors are the same for both band-processing estimations, since the damping factors are computed from the same identified modal parameters. The difference between BP2 and BP3 is

in the data used in Eq. 2.23 for the estimation of the $\tilde{a}_r$ coefficients. The band-processing method estimates the damping factors very well.

A noise level of 2% of the RMS value of the accelerance FRF was applied to each FRF. In addition, a random phase error was also included, with a maximum error of 2°. Results of the band-processing simulations using noisy data are presented in Table 3.11 and in Figs. 3.11 to 3.13. Notice in Fig. 3.11 that, when noise is applied to the signal, the algorithm tries to fit the data to the corresponding frequency band, and most of the roots are estimated to lie near the center of the frequency band. To aid in distinguishing these "noise modes," or "computational modes," an MPC criterion of 0.95 was used.
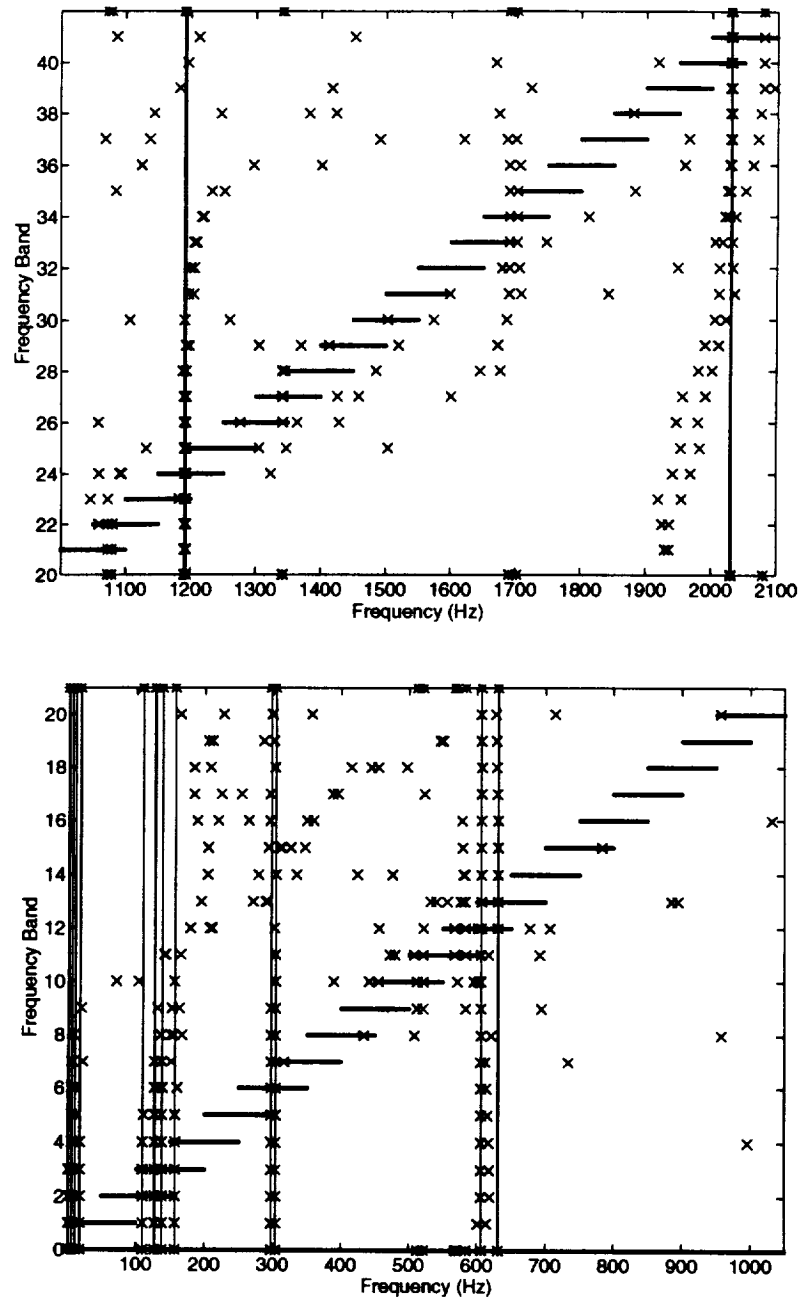
Figure 3.9: Estimated Natural Frequencies of 16-DOF Noise-Free Model Employing Band Processing

Table 3.9: Estimated Natural Frequencies — 16-DOF Noise-Free Models

Exact Freq. (Hz)	SSID Freq. (Hz)	SSID Percent Error	BP2 Freq. (Hz)	BP2 Percent Error	BP3 Freq. (Hz)	BP3 Percent Error
1.1564	1.1507	4.948e–01	1.1564	2.972e–05	1.1564	1.826e–05
6.0642	6.0628	2.430e–02	6.0642	2.348e–04	6.0642	8.340e–04
10.783	10.807	2.165e–01	10.783	1.096e–04	10.783	6.707e–06
18.127	18.115	6.439e–02	18.127	9.541e–05	18.126	1.658e–03
109.49	109.49	1.539e–03	109.49	3.223e–03	109.49	8.542e–04
127.14	127.15	7.669e–03	127.14	2.056e–03	127.14	1.502e–03
137.82	137.82	2.866e–03	137.81	6.636e–03	137.81	9.261e–03
156.87	156.86	5.341e–03	156.87	1.868e–03	156.87	4.088e–04
297.66	297.61	1.796e–02	297.26	1.345e–01	297.56	3.264e–02
304.47	304.41	1.745e–02	304.01	1.495e–01	304.50	1.125e–02
606.45	606.24	3.595e–02	605.12	2.202e–01	606.46	1.323e–03
631.08	626.89	6.648e–01	630.17	1.450e–01	629.75	2.110e–01
1190.4	1189.4	8.538e–01	1188.9	1.306e–01	1195.1	3.959e–01
1193.3	1192.3	8.922e–02	1191.1	1.872e–01	1196.4	2.525e–01
2029.1	2017.0	5.990e–01	2029.0	8.002e–03	2144.5	5.683e+00
2031.2	2017.6	6.686e–01	2031.8	2.758e–02	2171.2	6.893e+00

Table 3.10: Estimated Damping Factors — 16-DOF Noise-Free Models

| Exact	SSID		BP	
Damp.	Damp.	Percent	Damp.	Percent
Ratio	Ratio	Error	Ratio	Error
0.02	0.01980	1.022e+00	0.02000	2.688e−08
0.02	0.02104	5.179e+00	0.02000	1.833e−06
0.02	0.01824	8.789e+00	0.02000	4.289e−09
0.02	0.02055	2.754e+00	0.02000	1.311e−09
0.02	0.02009	4.696e−01	0.02000	4.131e−06
0.02	0.01882	5.911e+00	0.02000	2.508e−08
0.02	0.01993	3.678e−01	0.02000	7.951e−08
0.02	0.01993	3.481e−01	0.02000	1.177e−07
0.02	0.02157	7.847e+00	0.02000	3.463e−06
0.02	0.01980	9.997e−01	0.02000	4.913e−08
0.02	0.02018	8.870e−01	0.02000	1.115e−05
0.02	0.02593	2.964e+01	0.02000	2.233e−02
0.02	0.02031	1.552e+00	0.02000	1.140e−03
0.02	0.01923	3.830e+00	0.02000	3.208e−05
0.02	0.01549	2.257e+01	0.02000	1.718e−03
0.02	0.01571	2.145e+01	0.02000	2.260e−03
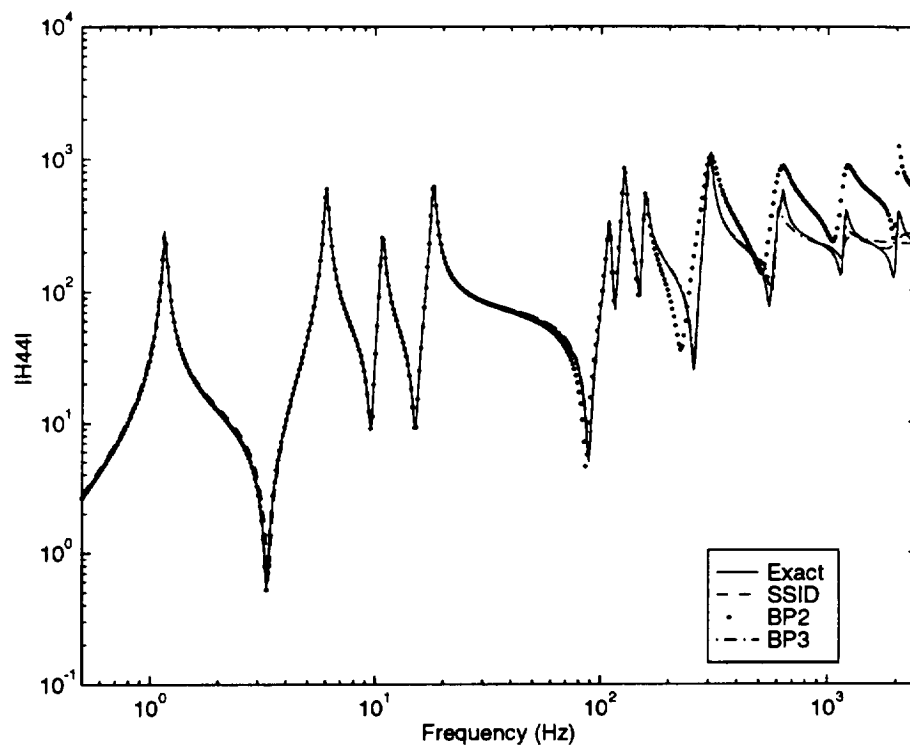
Figure 3.10: Comparison of FRFs of 16-DOF Noise-Free Models Using Band Processing

Table 3.11: Estimated Modal Parameters — 16-DOF Models Employing Band Processing with Noisy Data

| Exact Freq. (Hz)	BP2		BP3		Exact Damp. Ratio	BP Damp. Ratio	Percent Error
	Freq. (Hz)	Percent Error	Freq. (Hz)	Percent Error			
1.1564	1.1435	1.116e+00	1.4273	2.342e+01	0.02	0.00764	6.178e+01
6.0642	6.0579	1.054e–01	6.1922	2.110e+00	0.02	0.02016	7.789e–01
10.783	10.784	6.916e–03	12.538	1.629e+01	0.02	0.02046	2.296e+00
18.127	18.132	2.896e–02	19.005	4.846e+00	0.02	0.02143	7.152e+00
109.49	109.51	1.700e–02	109.51	1.989e–02	0.02	0.01880	5.985e+00
127.14	127.24	7.661e–02	127.39	2.013e–01	0.02	0.01977	1.168e+00
137.82	137.82	4.082e–04	137.80	1.642e–02	0.02	0.02009	4.474e–01
156.87	156.85	1.089e–02	156.87	9.918e–04	0.02	0.01996	1.836e–01
297.66	297.68	5.516e–03	297.92	8.773e–02	0.02	0.01987	6.248e–01
304.47	304.39	2.448e–02	304.04	1.415e–01	0.02	0.01975	1.239e+00
606.45	606.72	4.421e–02	606.75	4.916e–02	0.02	0.02058	2.911e+00
631.08	630.93	2.382e–02	631.76	1.073e–01	0.02	0.01957	2.145e+00
1190.4	1191.1	5.449e–02	1186.1	3.625e–01	0.02	0.02004	1.824e–01
1193.3	1193.1	2.350e–02	1192.0	1.118e–01	0.02	0.02000	1.637e–02
2029.1	2015.9	6.522e–01	2015.5	6.693e–01	0.02	0.01864	6.796e+00
2031.2	2031.8	2.709e–02	2054.4	1.141e+00	0.02	0.01896	5.213e+00
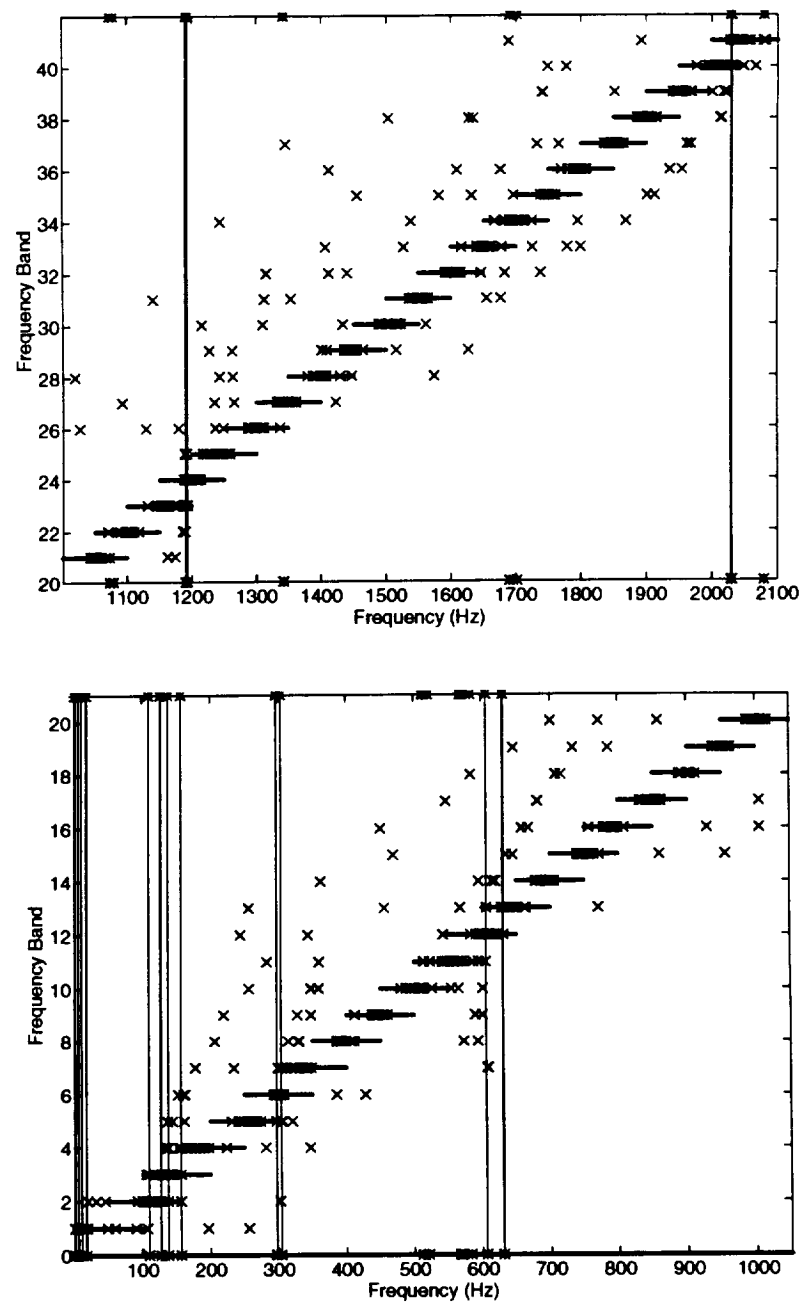
Figure 3.11: Estimated Natural Frequencies: Band Processing Using Noisy Data
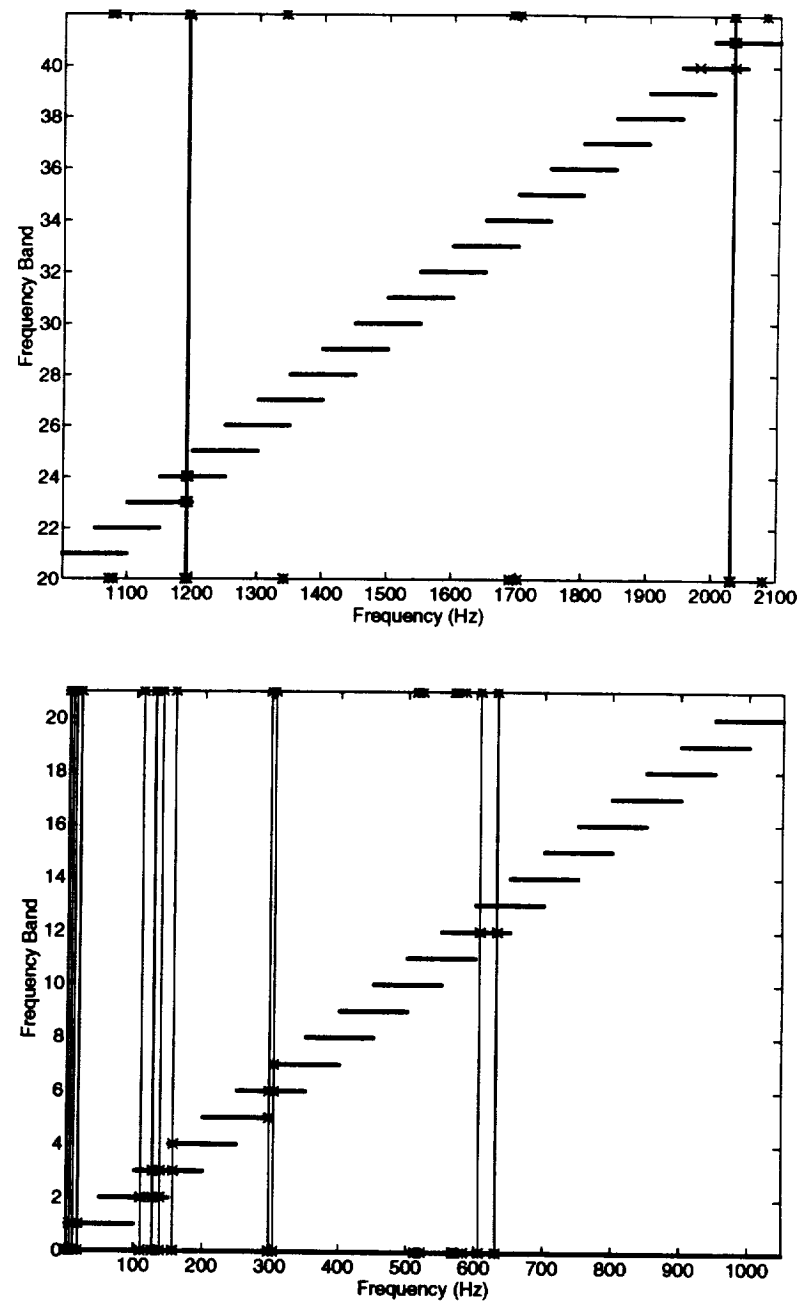
Figure 3.12: Estimated Natural Frequencies After Mode Selection: Band Processing Using Noisy Data

In Fig. 3.13, the BP2 approach estimates the FRF very well at low frequencies, while overestimating the response at higher frequencies, and it misses the 109 Hz mode. The converse is true for the BP3 approach; it underestimates the response at low frequencies while representing the response at high frequencies fairly well. The methods labeled BP2 and BP3 are only two possible approaches to processing the data; further research on this topic is needed.
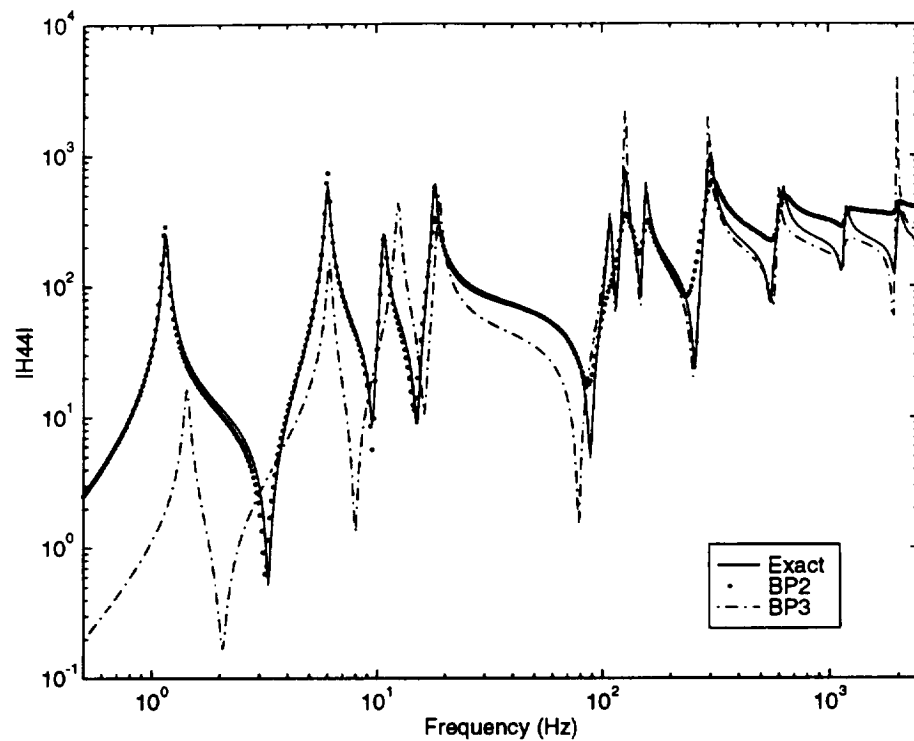

Figure 3.13: Comparison FRFs of 16-DOF Models Employing Band Processing with Noisy Data

These simulation results indicate that the modal parameters, Eq. 2.23, can be estimated band by band and then used for the final estimation of the system matrices. This is very encouraging, since no acceptable result was previously obtained using the original formulation of the SSID algorithm with this same noisy data. The band-processing approach was also applied to 12-DOF and 10-DOF reduced-order models with results similar to those presented here for the 16-DOF model. For further details, please see Ref. [1].

3.5.3 Conclusions

The following conclusions were reached:

- An algorithm that can potentially extend the range of usefulness of frequency-domain system identification has been proposed. The first stage of the algorithm employs processing of FRF data from a number of frequency bands of relatively limited bandwidth. It results in a collection of complex structural modes. The second stage of the algorithm then combines all of the complex structural modes into a single linear reduced-order system model (M, C, K).

- Band processing holds the potential of significant computational savings. Since the computations are done band by band with a much smaller amount of data, the frequency bands could be processed simultaneously on a parallel-processing computer. For tests where a large number of frequency lines are obtained, this could prove to be very cost effective.

Chapter 4

CONCLUSIONS AND RECOMMENDATIONS

Based on the research conducted under NASA Grant NAG8-1130 and summarized in this Final Report, the following conclusions may be drawn:

- The SSID Algorithm can successfully identify reduced-order mass, damping, and stiffness matrices of a substructure from noisy FRFs based on input-force data at all interface DOFs and acceleration data taken at all substructure DOFs.

- Except for the case of noise-free simulations, it is necessary to use the total least-squares method or the scaled total least-squares method for solving the overdetermined systems of linear equations; the ordinary least-squares method is not adequate.

- If there are more modes in the frequency bandwidth being considered than there are (acceleration) output sensor DOFs, it appears to be possible to employ pseudo degrees of freedom to expand the order of the model.

- If it is desired that the reduced-order model be valid over several decades of frequency, and if the number of (acceleration) output sensor DOFs is large enough to model the modes present in the data, then a band-processing procedure may be employed to identify a model that is valid over the entire bandwidth of the data.

- By adding a second coordinate transformation to the classical Craig-Bampton CMS modal transformation, a test-analysis model (TAM) can be created that is consistent with the original Craig-Bampton model.

During the course of research on the present grant, an attempt was made to use the SSID Algorithm to identify a model of the physical "Payload Simulator" in the Structural Dynamics Laboratory. That was not successful, probably because the measured data that was available was not taken over an appropriate bandwidth for the number of accelerometers that were used. Because of the amount of time that was required to get the SSID Algorithm to the state indicated by the conclusions stated above, it was not possible to complete this work on identifying a physical substructure or to develop a test/analysis plan for a complete test/identification program on a full-scale structure. Those Task 2 items are currently under investigation.

For the further development of the SSID algorithm, the following tasks are recommended:

- Develop a computer program for applying the SSID algorithm to full-scale Space Shuttle payloads. This will include further refinement of the use of least-squares solvers and band processing.

- Apply the SSID algorithm to identify math models of representative physical structures, starting with the "Payload Simulator" in the Structural Dynamics Laboratory at UT-Austin.

- Assess various methods for measuring dynamic reactions and develop design criteria for reaction-measurement systems.

BIBLIOGRAPHY

[1] Blades, E. L., and Craig, R. R., Jr., *A Frequency-Domain Substructure System Identification Algorithm*, Report CAR 96-2, Center for Aeromechanics Research, Bureau of Engineering Research, The University of Texas at Austin, August 1996. (Also Blades, E. L., M.S. Thesis, The University of Texas at Austin, August 1996.)

[2] Craig, R., and Blades, E., "Substructure System Identification – Reduced-Order Models," *3rd International Conf. on Dynamics and Control of Structures in Space*, London, England, May 1996.

[3] Blades, E. L., and Craig, R. R., Jr., "Frequency-Domain Substructure System Identification," *Proc. 15th International Modal Analysis Conference*, Orlando, FL, Feb. 1997, pp. 34-40.

[4] Blades, E. L., and Craig, R. R., Jr., "A Craig-Bampton Test-Analysis Model," *Proc. 15th International Modal Analysis Conference*, Orlando, FL, Feb. 1997, pp. 1386-1391.

[5] Craig, R. R., Jr., and Blades, E. L., "A Band-Processing Algorithm for Structural System Identification," Paper No. AIAA-97-1039, *Proceedings AIAA/ASME/ASCE/AHS/ASC 38th Structures, Structural Dynamics, and Materials Conference*, Kissimmee, FL, April 1997.

[6] Craig, R. R., Jr., Cutshall, W. K., and Blades, E. L., *A New Substructure System Identification Method*, Report CAR 95-1, Center for Aeromechanics Research, Bureau of Engineering Research, The University of Texas at Austin, December 1995.

[7] Craig, R. R., Jr., *Math Model Verification and Updating Based on Measured Excitations and Reactions*, Report CAR 95-2, Center for Aeromechanics Research, Bureau of Engineering Research, The University of Texas at Austin, December 1995.

[8] Craig, R. R., Jr., "A New Substructure System Identification Algorithm," Paper No. AIAA-95-1298-CP, *Proceedings AIAA/ASME/ASCE/AHS/ASC 36th Structures, Structural Dynamics, and Materials Conference*, New Orleans, LA, April 1995, pp. 1209-1217.

[9] Cutshall, W. K., and Craig, R. R., Jr., "Simulation Results, Including Noisy Data, for a New Substructure System Identification Method," *Proceedings 13th International Modal Analysis Conference*, Nashville, TN, February 1995, pp. 1805-1811.

[10] Craig, R. R., Jr., Blades, E. L., and Cutshall, W. K., "A Reduced-Order Substructure System Identification Method," Paper No. AIAA-96-1200-CP *Proceedings AIAA Dynamics Specialists Conf.*, Salt Lake City, UT, April 1996 pp. 12-20.

[11] Craig, R. R., Jr., and Bampton, M.C.C., "Coupling of Substructures for Dynamic Analysis," *AIAA Journal*, Vol. 6, No. 7, July 1968, pp. 1313-1319.

[12] Craig, R. R., Jr., Kurdila, A. J., and Kim, H. M., "State-Space Formulation of Multi-Shaker Modal Analysis," *Int. J. Analytical and Experimental Modal Analysis*, Vol. 5, No. 3, July 1990, pp. 169-183.

[13] Van Huffel, S. and Vandewalle, J., *The Total Least Squares Problem: Computational Aspects and Analysis*, Society of Industrial and Applied Mathematics, Philadelphia, 1991.

[14] *MATLAB*™, The MathWorks, Natick, MA, 1991.

[15] Kammer, D. C., "Sensor Placement for On-Orbit Modal Identification and Correlation of Large Space Structures," *Journal of Guidance, Control, and Dynamics*, Vol. 14, No. 2, March–April 1991, pp. 251–259.

[16] Guyan, R., J., "Reduction of Stiffness and Mass Matrices," *AIAA Journal*, Vol. 3, No. 2, Feb. 1965, p. 380.

[17] Huang, H. H., and Craig, R. R., Jr., "System Identification and Model Updating for Substructures," *Report CAR 92-1*, Center for Aeromechanics Research, The University of Texas at Austin, April 1992.

[18] Kammer, D. C., and Flanigan, C. C., "Development of Test-Analyis Models for Large Space Structures Using Substructure Representations," *Journal of Spacecraft and Rockets*, Vol. 28, No. 2, March–April 1991, pp. 244–250.

[19] Craig, R. R., Jr, and Bampton, M. C. C., "On the Iterative Solution of Semidefinte Eigenvalue Problems," *The Aeronautical Journal of the Royal Aeronautical Society*, Vol. 75, No. 724, April 1971, pp. 287–290.

[20] Lembregts, F., Leuridan, J., and Van Brussel, H., "Frequency Domain Direct Parameter Identification for Modal Analysis: State Space Formulation," *Mechanical Systems and Signal Processing*, Vol. 4, No. 1, 1990, pp. 65–75.

[21] *CADA-X Modal Analysis Manual*, Sect. 3.9, LMS International, Leuven, Belgium.

Appendix A

SSID EXAMPLE

This appendix provides an example case from Chapter 6 of CAR 96-2[1], a report entitled, *A Frequency-Domain Substructure System Identification Algorithm.*

A.1 Example Case from CAR 96-2

For this example, the MATLAB algorithm ebr4.m was run for a 16-DOF damped model with no noise and with a 300 Hz frequency spectrum. The following checklist details the inputs needed to set up this example.

- **No Noise:** To remove the noise input to the algorithm, set magnoise = 0, phnoise = 0, and nsample = 1. Additionally, comment out the call to the function applynoise and uncomment the line under it, "Abn = AB; Pn = P."

- **16 DOF:** To apply the algorithm to a 16 DOF model, comment out all of the "modes =" lines except the line, "modes = [1:10,17,18,21,22,29,30]";

- **300 Hz:** To test the system over a 300 Hz frequency spectrum with 512 frequency lines, set ne = 512 and fmax = 300.

These inputs are all that is required to run the example mentioned above. The following pages present the algorithm used for this example, set up as

presented in the list above, as well as an output diary from the execution of the algorithm. Note that the numbers in the output diary match those presented in Tables. 6.8 and 6.9 in CAR 96-2.

A.2 MATLAB Program ebr4.m for 16 DOF, No Noise, 300 Hz

This MATLAB program was developed by Eric Blades in the course of his research for the M.S. degree at The University of Texas at Austin. It is a "research" implementation of the SSID Algorithm with Model Reduction (SSID-MR).

```
% EBr4  (6/2/96)      ***Minv*K and Minv*C from Single Test***
%                     ***               M, C, and K                    ***
%
%   *Damped System and No Noise
%   *Ordinary LS Estimate Based on [M +1/(j*W)C -1/W^2*K]A=P.
%   *Ordinary LS Estimate Based on Complex Data and also on R/I data.
%   *THREE Active Forces, F, Used to Generate Response
%       Vectors, X, and NO Reaction Forces, R.
%   *Modification of WC32 for use with larger models, PS1 (52 DOF).
%   *NO Test Stand
%   *Active Forces and Reactions Enter into Final Estimate of Minv*K
%       and Minv*C.
%
% Set Parameters:
%    ne = No. excitation freqs. (squared)
%    nx = No. of DOF of Substructure Model  (? =#of measurements)
%    nf = No. of Active Forces
%    nr = No. of Reactions
%    ns = No. of States
%    nb = No. of DOF of Substructure and Test Stand
%    nsample = No. of samples of exitation source
%
clear
rand('seed',0);
echo off
load /home/grad/shawnvdw/blades/ps1.mat %  Load in M and K
```

```
%
na=size(KA,1);
df=.02;    % Damping Factor
[phia,eiga]=massnorm(KA,MA); %  Mass-normalize evecs
freqa=sqrt(eiga)/(2*pi); w=sqrt(eiga);
[CA,zetaa]=damping(MA,KA,ones(na,1)*df); %  Modal damping matrix
%
% Forced DOF: 10 22 and 50
% Reaction DOF: NONE
fdof=[10 22 50];
nf=3;
nr=0;
nd=nf+nr;
%
% "Preserve" these modes of the "A" Structure
%modes=[1:52]; %  All modes
modes=[1:10,17,18,21,22,29,30];    %  16 DOF Model
%modes=[1:10,17,18];                %  12 DOF Model
%modes=[1:10];                      %  10 DOF Model
%
% DOF to OMIT from the Model--All the X and Y Rotations
rdof=eidv(phia(:,modes),[1:na]',length(modes));
odof=omitdof(na,rdof);
%
% DOF to RETAIN from the Model
[rdof,ridof,frdof]=keptdof(na,odof,fdof(1:nf),fdof(nf+1:nd));
%rdof=[1:52]; frdof=fdof;            %  All modes
%
% Size of the substructure to identify
nx=length(rdof);
ns=2*nx;
%
%  Input Test Frequencies
ne=512; %  Number of excitation freqs
deltaf=1;
for count=1:1
fmin=1.0;
fmax=300; %  max frequency for test
Freq=linspace(fmin,fmax,ne);
[Freq(1) Freq(ne) Freq(2)-Freq(1) ne]
W=Freq*2*pi;
W2=W.^2;
%
% Noise parameters
```

```
nsample=1;
magnoise=0;
phnoise=0;
tol1=1e-10;
tol2=1e-10;
%
% Initialize
DA=zeros(na,(nf+nr));
DAr=zeros(nx,(nf+nr));
for n=1:nd
  k=fdof(n);
  DA(k,n)=1;
  k=frdof(n);
  DAr(k,n)=1;
end
%
%variables=[nf, nsample, magnoise, phnoise, tol1, tol2];
%[KHA,CTHETAE,CLAMAE,AA,Hrf]=stls(Freq,MA,CA,KA,rdof,fdof,[],variables);
%
% Form Frequency-Response Vectors (Direct Solution)
[AB,P]=frfdirect(W,MA,CA,KA,DA);
%
% Simulate Noise
%[ABn,Pn]=applynoise(AB,P,nsample,magnoise,phnoise);
ABn=AB; Pn=P;
%
% Remove Response Vectors Corresponding to "A" Structure
AA=ABn(rdof,:);
%
% Form Velocity and Displacement FRFs
[AA,VA,XA,Hff]=calvxf(AA,Pn,Freq);
%
VXFA=[VA;XA;-Hff];                          %  LHS of Eqn 3.7
%
% Form Real/Imaginary Partitions
AA2=[real(AA) imag(AA)];                     %  RHS of Eqn 3.7
VXFA2=[real(VXFA) imag(VXFA)];
%
% Step 1--Identification of M^-1K and M^-1C and the resulting eigensolution
% Solve Equation 3.7
CKDAE2=-AA2/VXFA2;
%
% Complex Eigensolution Based on Estimated Minv*C and Minv*K
CHA=CKDAE2(:,1:nx);
```

```
KHA=CKDAE2(:,nx+1:ns);
%
% Equation 3.11
ASAHATE=[CHA eye(nx);eye(nx) zeros(nx)];
BSAHATE=[KHA zeros(nx); zeros(nx) -eye(nx)];
%
% Equation 3.12;   Lambda=LambdaHat
[CTHETAE,CLAMAE]=eig(-BSAHATE,ASAHATE);
[CTHETAE,CLAMAE]=eigensorti(CTHETAE,diag(CLAMAE));
%
[phikm,eigkm]=eig(KHA);
[phikm,eigkm]=eigensortr(phikm,diag(eigkm));
zetass=-real(CLAMAE)./abs(CLAMAE);
omegss=imag(CLAMAE)./sqrt(1-zetass.^2);
[CLAMAE(1:nx) CLAMAE(nx+1:ns)];
[zetaa(modes) zetass(1:nx)]
[freqa(modes) omegss(1:nx)/(2*pi) sqrt(eigkm)/(2*pi)];
freqmk(:,count)=sqrt(eigkm)/(2*pi);
freqss(:,count)=omegss(1:nx)/(2*pi);
end
%
% Make room, clear some variables
clear CKDAE2 VXFA2 AA2 ASAHATE BSAHATE ABn P Pn
%
% Step 2--Identification of M, C, and K
%
% Estimation of Inverse Generalized Modal Parameters a_r
% Equation 3.23
CTX=CTHETAE(1:nx,:);
%
[E,Y]=caley(AA,CLAMAE,CTX,DAr,Freq);
%
% Inverse Generalized Mass Estimation
% Solving Equation 3.23 for 1/~a.
%
GASAIE=E\Y;
clear E Y CTX
%
% Estimated Generalized Modal Parameter Vector -- a_r
GASAE=1./GASAIE;
%
% Estimated Generalized Modal Parameter Vector -- b_r
% Solving Equation 3.25 for ~b.
GBSAE=-CLAMAE.*GASAE;
```

```
%
% Forming (Thetahat)^-1
CTHI=inv(CTHETAE);
%
% Estimated State-variable A Matrix
% Equation 3.26a
ASAE=CTHI.'*diag(GASAE)*CTHI;
%
% Estimated State-variable B Matrix
% Equation 3.26b
BSAE=CTHI.'*diag(GBSAE)*CTHI;
%
% Extract System Matrices
M1=rmvsm(real(ASAE),1,nx+1,nx,nx);
M2=rmvsm(real(ASAE),nx+1,1,nx,nx);
M3=-rmvsm(real(BSAE),nx+1,nx+1,nx,nx);
M=M3;
C=rmvsm(real(ASAE),1,1,nx,nx);
K=rmvsm(real(BSAE),1,1,nx,nx);
C2=damping(M,K,zetass(1:nx));
[phie,eige]=eig(K,M);
[phie,eige]=eigensortr(phie,diag(eige));
for k=1:nx
  phie(:,k)=real(phie(:,k)/sqrt(sum(phie(:,k).^2)));
end
freqe=sqrt(eige)/(2*pi);
masse=sum(sum(M));
m=diag(phie'*M*phie);
c=diag(phie'*C*phie);
k=diag(phie'*K*phie);
zetae=c./(2*m.*sqrt(eige));
mace=mac(phia(rdof,1:30),phie);
[y,ind]=max(mace);
%[zetaa(modes) zetae]
[freqa(modes) freqe]
[y;ind]
%
% Compare FRF's (due to force 1) to exact
f=1;
Freqp=logspace(log10(.5),log10(2500),512); Wp=Freqp*2*pi;
[AAp,p]=frfdirect(Wp,MA,CA,KA,DA(:,f));
[AAe,p]=frfdirect(Wp,M,C,K,DAr(:,f));
[AAe2,p]=frfdirect(Wp,M,C2,K,DAr(:,f));
figure(1)
```

```
loglog(Freqp,abs(AAp(fdof(f),:)),Freqp,abs(AAe(frdof(f),:)),'g-.')
hold on
loglog(Freqp,abs(AAe2(frdof(f),:)),'r.')
hold off
```

A.3 MATLAB Output Diary for 16 DOF, No Noise, 300 Hz

ans =

Frequency Input Spectrum
Table 6.3   row #1

1.0000 300.0000   0.5851 512.0000

ans =

Estimated Damping Factors
Table 6.9   columns #1,2

0.02	0.02000
0.02	0.02000
0.02	0.02000
0.02	0.02000
0.02	0.02000
0.02	0.02000
0.02	0.02000
0.02	0.02000
0.02	0.02000
0.02	0.02000
0.02	0.02000
0.02	0.01996
0.02	0.01775
0.02	0.02024
0.02	0.02135
0.02	0.02094

ans =

Estimated Natural Frequencies
Table 6.8   *columns #1,2*

1.1564	1.1564
6.0642	6.0642
10.783	10.783
18.127	18.127
109.49	109.49
127.14	127.14
137.82	137.82
156.87	156.87
297.66	297.66
304.47	304.47
606.45	606.15
631.08	613.54
1190.4	1047.1
1193.3	1159.3
2029.1	1526.7
2031.2	1682.3

ans =

Maximum MAC Values
Table 6.10   *columns #2,3*

Columns 1 through 7

1.0000	1.0000	1.0000	1.0000	1.0000	1.0000	1.0000
1.0000	2.0000	3.0000	4.0000	5.0000	6.0000	7.0000

Columns 8 through 14

1.0000	1.0000	1.0000	0.9987	0.9344	0.6239	0.6639
8.0000	9.0000	10.0000	17.0000	18.0000	20.0000	21.0000

Columns 15 through 16

0.6561	0.6063
16.0000	27.0000